# POLITECNICO DI TORINO

## MASTER's Degree in Areospace Engineering


SIEMENS

## MASTER's Degree Thesis

# Image-Based Methods for Investigating the Dynamic Behavior of Space Structures under Multiaxial Loads

**Supervisors**

Prof. Enrico ZAPPINO

Eng. Davide MASTRODICASA

Dott. Alberto GARCIA DE MIGUEL

Eng. Ruben ARAUJO

**Candidate**

**Andrea CAVAGNOLO**

**October 2025**

**Image-Based Methods for Investigating the Dynamic Behavior of Space Structures under Multiaxial Loads**

**Andrea Cavagnolo**

**Abstract**

In the aerospace industry, component characterisation and validation are essential to ensuring structures' safety, reliability, and performance in orbit or critical environments. Traditional structural testing methodologies, such as vibration control in electrodinamic shakers and experimental modal analysis, are well-established tools for studying systems' dynamic and modal properties. However, they require dedicated instrumentation, long preparation times, and complex experimental setups, increasing development costs. In parallel, Digital Image Correlation (DIC) has emerged as a highly accurate optical technique. It is also useful for avoiding the use of accelerometers on lightweight components. Nevertheless, it presents significant limitations: it requires random patterns on the surfaces under analysis, generates large volumes of data, and involves long processing times, reducing its efficiency in contexts where speed and flexibility are critical.

In this scenario, the present thesis, developed in collaboration with Siemens Industry Software NV in Leuven, investigates the application of the Video Motion Magnification (VMM) methodology, an innovative image-based approach. This work implements a multi-stage workflow, progressing from preliminary academic research on a generic plate (using a rudimental test setup) to industrial simulation and subsequent experimental investigation on a CubeSat dummy model, to effectively assess VMM's utility.

In a preliminary phase, virtual image sequences generated in Blender were used as a pre-test tool to evaluate optimal camera positioning, estimate the displacement noise floor, and assess the expected dynamic response before performing physical measurements. Once validated in the virtual environment, VMM was applied to the experimental setup as a quick pre-test analysis before executing the complete vibration campaign with conventional sensors. This approach enables the visualisation and amplification of small motions and deformations that are not perceptible to the naked eye, starting from video sequences acquired with standard cameras.

It allows the fast and noninvasive extraction of qualitative information on the structure's dynamic behaviour while significantly reducing the level of instrumental complexity compared to traditional measurement methods. The absence of dedicated markers and the ability to operate directly on easily acquired video data further enhance VMM's versatility. The case study focused on a 3D-printed dummy model of a CubeSat, subjected to a Random Control Test. The application of VMM enabled the visualisation and interpretation of the main operational deflection shapes, verification of boundary conditions, and qualitative characterisation of structural behaviour during the pre-testing phase. The results demonstrate that VMM can effectively reduce experimental preparation time and resource usage, while maintaining adequate reliability to support preliminary design validation. Overall,

this work confirms the potential of VMM as a complementary pre-test and diagnostic tool alongside traditional modal and vibration analysis techniques.

# ACKNOWLEDGMENTS

I would like to express my sincere gratitude to Professor Enrico Zappino for his invaluable guidance and instruction during the preliminary phase of this thesis. His proactive approach, expertise, and support were instrumental in helping me proceding with this project. Professor Zappino's mentorship provided a solid foundation for my research, and I am particularly grateful for his insightful suggestions that shaped the direction of my work.
I extend my deepest appreciation to Eng. Davide Mastrodicasa for being an exceptional on-site supervisor. Upon my arrival in Belgium, Davide provided comprehensive training and guidance, clarifying the intricate processes involved in the VMM technique. His availability, clear explanations, and patient instruction were crucial to my understanding and successful integration into the project.
A special note of thanks goes to Dott. Alberto Garcia de Miguel, who meticulously guided me through the theoretical aspects and preparation of my work. He consistently provided valuable information and direction throughout the entire project, and despite the physical distance, he remained an ever-present supervisor. His steadfast belief in my abilities was incredibly motivating, and his timely feedback and encouragement proved invaluable, especially during challenging theoretical considerations.
I am also profoundly grateful to Eng. Ruben Arujo for his expert assistance during the critical setup phase of the test on the 4-DOF platform. His technical proficiency and willingness to troubleshoot ensured that I had a stable and functional environment for my experimental work, which was essential for the progress of my thesis.
Finally, I would like to thank the Politecnico di Torino and Siemens Digital Industry NV for providing outstanding instrumentation and resources throughout this endeavor. The comprehensive knowledge and rigorous education I received during my Master's program laid the groundwork for this research. The supportive academic environment and access to state-of-the-art facilities were indispensable for the successful completion of my thesis.

# Table of Contents

# List of Figures

# List of Tables

# Chapter 1

# Theoretical Foundations and Principles of Dynamic Testing

## 1.1 Theoretical Foundations of Mechanical Vibrations

### 1.1.1 Introduction to the Phenomenon of Mechanical Vibration

Any motion that repeats itself after an interval of time is called a Vibration Oscillation (source [1]). The motion of a pendulum or a plucked string in a guitar is an example of vibratory motion. Generally, a vibrating system has a means of storing kinetic energy (a mass element) coupled with potential energy storage (an elastic element), along with a damper that dissipates the energy available in the system. During vibration the available potential energy is converted to kinetic energy or vice versa (Figure 1.1). If the system is affected by damping, its total energy and vibration amplitude will reduce until it stops. If damping exists, an external energy source is always required to maintain the vibratory motion.

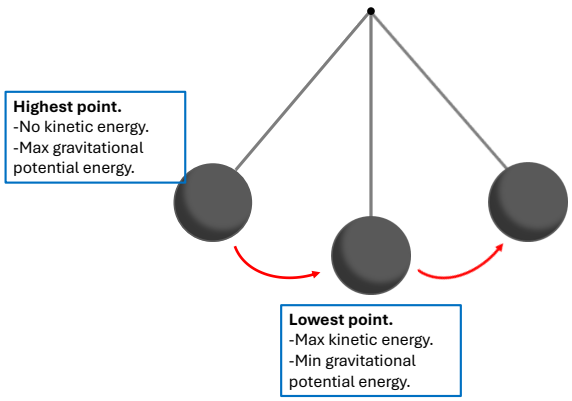


**Figure 1.1:** Pendulum's motion.

Vibrations in general occur in almost all mechanical systems to some magnitude. Therefore, researchers concentrated on understanding this natural phenomenon and developing mathematical theories to describe physical systems. It may be a significant factor for consideration or not, and lead to detrimental or catastrophic situations, like:

- Excessive vibrations during the operation of pumps and other machines can lead to operational inefficiencies.
- Natural causes can induce vibration, such as earthquakes or wind bursts, which can build up stresses in structures like high-rise buildings, bridges, etc.
- Vibration induced by an imbalance in the engine can lead to the failure of the machine while rotating.
- Comfort of passengers in a car on a dumpy road.

There are examples where vibratory oscillation is beneficial.

- Mechanical clocks, musical instruments, and loudspeakers use the basis of vibrations to function.
- Ultrasonic probes used in medical and nondestructive testing applications.
- Techniques in certain machining, casting, forging, and welding processes that improve efficiency include vibration-assisted approaches such as Ultrasonic Assisted Machining, Vibration-Assisted Forging, Vibratory Stress Relief, and Ultrasonic-Assisted Welding.
- Devices that can warn and register seismic events.

### 1.1.2 Fundamental Concepts and Terminology in Vibration Analysis

The **Natural Frequency** of a system is the frequency at which it would vibrate if it were allowed to move freely without an external force applied. It is also known as the characteristic frequency, resonant frequency, or normal frequency.
The deformed shape of the structure at a specific natural frequency is named as its **Mode Shape** of vibration. A given mode shape is a unique characteristic of the respective natural frequency. The term mode shape is also known as normal mode, characteristic mode and fundamental shape. When a system is excited it vibrates in a specific manner determined by its geometry, material properties, and boundary conditions. The mode shapes describe how different system parts move relative to each other during vibration.
When the system's natural frequency coincides with the frequency at which the external force/load is oscillating, then **Resonance** occurs. At resonance, the system vibrates with excessive amplitudes that can lead to failure.
The collapse in 1940 of the Takoma Narrows Bridge (Figure 1.2) is a famous example of aeroelastic flutter, where the wind loads induced a resonant vibration.

**Figure 1.2:** Takoma Bridge collapse (source [2]).

### 1.1.3 Degrees of Freedom: Definition, Classification, and Analytical Considerations

> *"The minimum number of independent parameters required to determine completely The positions of all parts of a system at any instant of time define the number of degree of freedom of a system."[1]*

We aim to simplify systems to the lowest number of Degrees Of Freedom (DOF) for the sake of the analysis.

Anyway, we must remember that in real-life scenarios, structures are defined by infinite

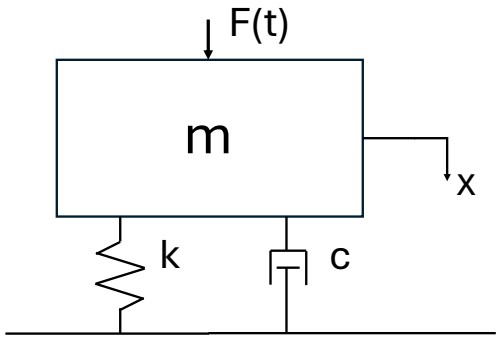


**Figure 1.3:** one DOF.

degrees of freedom. Those systems are defined as continuous systems, while we tend to describe them by a finite number of elements; therefore, they are defined as discrete systems. The current state of the art in numerical solution methods provides more accurate

evaluations when the number of elements is high (i.e., when a finer mesh is used), at the cost of increased computational effort and longer processing times.

### 1.1.4 Formulation of Equations of Motion for SDOF and MDOF Systems

As discussed in the previous section, systems with a single degree of freedom are easy to solve and useful for understanding better system vibration behaviour. Single degree of freedom (**SDOF**) models are usually modelled with a spring, a damper and a mass. For simplicity, it is usually assumed that the spring and the damper are massless. The mass $m$ moves only vertically and a time-dependent vertical force *F(t)* acts on the mass $m$. By analysing, using Newton's laws, the free body diagram (Figure 1.3), and reorganizing the terms of the equation, we can derive the equation of motion for an SDOF model:

$$m\frac{d^2x(t)}{dt^2} + c\frac{dx(t)}{dt} + kx(t) = F(t)$$

For a discrete dynamic system, including more than one DOF is necessary. Because of this, we move into Multi Degree of Freedom (**MDOF**) systems. Even though the system becomes complex, the resulting equations of motion can be simplified by applying several assumptions.

$$\mathbf{M}\frac{d\mathbf{x(t)}^2}{dt^2} + \mathbf{C}\frac{d\mathbf{x(t)}}{dt} + \mathbf{Kx(t)} = \mathbf{F}(t)$$

**M** is the mass matrix, **K** is the stifness matrix, **C** is the damping matrix. The vector **x(t)** is the displacement vector and **F**(t) is the load vector. If there are $n$ degrees of freedom in the system, the matrices will have the dimensions of $n\mathbf{x}n$ and the vectors of dimensions $1\mathbf{x}n$.

### 1.1.5 Principles and Methodology of Modal Analysis

As established in the previous section, the motion of an MDOF system is described by a set of coupled matrix differential equations:

$$\mathbf{M}\ddot{\mathbf{x}}(t) + \mathbf{C}\dot{\mathbf{x}}(t) + \mathbf{K}\mathbf{x}(t) = \mathbf{F}(t) \tag{1.1}$$

The presence of off-diagonal terms in the mass (**M**), damping (**C**), and stiffness (**K**) matrices implies that the equations are coupled. Solving this system directly is computationally intensive and offers little physical insight into the system's intrinsic behavior.
Modal Analysis is a powerful fundamental technique to transform this complex, coupled system into a simple, uncoupled SDOF set. This is achieved by changing the coordinate system from the physical coordinates $\mathbf{x}(t)$ (the displacements of the masses) to a new set of generalized coordinates known as modal coordinates $\mathbf{q}(t)$.
First, the system, in undamped and with external forces set to zero, needs to be solved($\mathbf{C} = \mathbf{0}$, $\mathbf{F}(t) = \mathbf{0}$). The so-called Eigenvalue Problem consists of obtaining the structure's Natural Frequencies and Mode Shapes.

$$\mathbf{M}\ddot{\mathbf{x}}(t) + \mathbf{Kx(t)} = \mathbf{0} \tag{1.2}$$

As shown in the book [1], by assuming a harmonic solution of the form $\mathbf{x}(t) = \Phi \sin(\omega t + \psi)$, we can derive the generalized eigenvalue problem:

$$\left([\mathbf{K}] - \ \omega_i^2 \, [\mathbf{M}]\right) \{\Phi\}_i = \mathbf{0} \tag{1.3}$$

Solving this problem yields the system's fundamental dynamic characteristics. The solutions consist of the eigenvalues $(\omega_1^2, \omega_2^2, \ldots, \omega_n^2)$, which computed return the system's Natural Frequencies ($f_i = \frac{\omega_i}{2\pi}$), and the corresponding eigenvectors $(\Phi_1, \Phi_2, \ldots, \Phi_n)$, which represent the Mode Shapes of vibration.

The mode shapes obtained from the eigenvalue problem possess a crucial mathematical property known as Orthogonality. With respect to the mass and stiffness matrices, the mode shapes satisfy the following relationships

$$for \quad i \neq j : \Phi_i^T \mathbf{M} \Phi_j = 0 \qquad and \qquad \Phi_i^T \mathbf{K} \Phi_j = 0. \tag{1.4}$$

When the indices are equal ($i = j$), the products define the scalar quantities known as Modal Mass and Modal Stiffness:

$$m_i^* = \Phi_i^T \mathbf{M} \Phi_i \quad \text{(Modal Mass)} \qquad k_i^* = \Phi_i^T \mathbf{K} \Phi_i \quad \text{(Modal Stiffness)}$$

This principle is the mathematical key that permits the decoupling of the equations of motion.

The core of modal analysis is the coordinate transformation. The physical displacement vector $\mathbf{x}(t)$ can be expressed as a linear superposition of the mode shapes, where the contribution of each mode is weighted by its corresponding modal coordinate $q_i(t)$:

$$\mathbf{x}(t) = \Phi_1 q_1(t) + \Phi_2 q_2(t) + \cdots + \Phi_n q_n(t) = \mathbf{\Phi q}(t) \tag{1.5}$$

Here, $\mathbf{\Phi}$ is the Modal Matrix, whose columns are the mode shape vectors $\Phi_i$. By substituting this expression into the whole equation of motion and pre-multiplying by the transpose of the modal matrix, $\mathbf{\Phi}^T$, the orthogonality conditions are leveraged to diagonalize the system matrices. This yields a new set of equations in modal coordinates:

$$\mathbf{M}^* \ddot{\mathbf{q}}(t) + \mathbf{C}^* \dot{\mathbf{q}}(t) + \mathbf{K}^* \mathbf{q}(t) = \mathbf{F}^*(t) \tag{1.6}$$

In this equation, $\mathbf{M}^* = \mathbf{\Phi}^T \mathbf{M} \mathbf{\Phi}$ is the diagonal modal mass matrix, $\mathbf{K}^* = \mathbf{\Phi}^T \mathbf{K} \mathbf{\Phi}$ is the diagonal modal stiffness matrix, and $\mathbf{F}^*(t) = \mathbf{\Phi}^T \mathbf{F}(t)$ is the modal force vector.

Proportional Damping, of the form $\mathbf{C} = \alpha \mathbf{M} + \beta \mathbf{K}$. These coefficients ($\alpha$ and $\beta$) are known as Rayleigh damping coefficients, typically determined by specifying two modal damping ratios ($\zeta_i$) at two distinct natural frequencies ($\omega_i$) of the system. This allows calculating $\alpha$ and $\beta$ through two linear equations, guaranteeing a diagonal modal damping matrix. This assumption ensures that the modal damping matrix $\mathbf{C}^* = \mathbf{\Phi}^T \mathbf{C} \mathbf{\Phi}$ also becomes diagonal.

With the matrices now diagonal, the system is reduced to a set of $n$ independent SDOF

equations, one for each mode $i$:

$$m_i^* \ddot{q}_i(t) + c_i^* \dot{q}_i(t) + k_i^* q_i(t) = f_i^*(t) \tag{1.7}$$

These equations can be solved independently for their modal coordinate $q_i(t)$.
Once the solution for each modal coordinate is found, the final physical response of the system is obtained by transforming back to the original coordinates via the principle of Modal Superposition:

$$\mathbf{x}(t) = \sum_{i=1}^{n} \Phi_i q_i(t) \tag{1.8}$$

In large-scale models (e.g., Finite Element Analysis), the first few low-frequency modes often dominate the dynamic response. By using Modal Truncation, which consists of calculating and superimposing the responses of only these dominant modes, engineers can obtain a highly accurate approximation of the system's behavior at a significantly reduced computational cost.

## 1.2 Physical Testing: Objectives, and Test Tailoring

### 1.2.1 The Imperative of Physical Testing

The validation of engineered systems through environmental testing is a critical step in high-reliability sectors such as aerospace, defense, and automotive. It aims to reproduce a real-world dynamic environment within a controlled laboratory setting to determine a product's structural and functional robustness.
This empirical validation serves multiple purposes throughout the product lifecycle (Figure 1.4 source [3]):

- is employed during initial development to uncover design weaknesses
- is used for a formal qualification to certify that a product meets contractual or regulatory specifications
- assesses long-term durability and fatigue life
- serves as a screening tool in production operations to detect manufacturing defects

Testing is used to provide a high degree of confidence that a product will survive and function reliably in its operational environment, as discussed in detail in the Conference [4].
The principle of **Test Tailoring** is essential for modern environmental testing procedures. On one hand, the test must be sufficiently severe to precipitate potential field failures, as a lack of severity leads to undertesting, a condition that risks leaving genuine design vulnerabilities undetected and can result in catastrophic in-service failures.
On the other hand, the process must avoid introducing unrealistic loads that would induce failures that are not representative of the operational environment, a condition known as overtesting.
Test Tailoring is a systematic process wherein the test procedures and parameters are

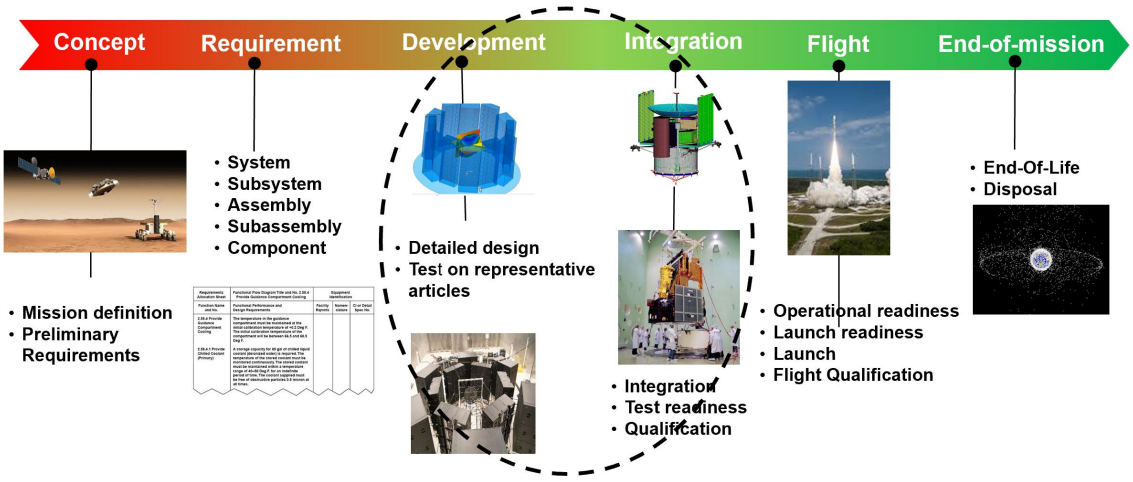


**Figure 1.4:** Life cycle of a space product.

analytically derived and specified to accurately represent the damage potential of the product's intended environment and prove that the hardware can survive a controlled and representative simulation of its operational life.

#### 1.2.1.1 The Role of Standards and In-Field Data

Standards provide a robust, repeatable baseline for qualification. However, a significant evolution in the discipline has been the shift towards more realistic testing profiles derived from recorded in-field data accordingly to the Article [5].
While standards provide a generalized envelope of an environment, they may not capture the specific, unique dynamic events that a product will experience. Advanced data acquisition and processing techniques now allow engineers to capture real operational vibration data and use it to synthesize a test profile. This data-driven approach is best exemplified by **Time Waveform Replication (TWR)**, a methodology that seeks to reproduce the exact time history of a measured event in the laboratory. On the other hand, a Random Control Test uses statistical analysis of operational measurements to create an enveloping Power Spectral Density (PSD) profile, ensuring the component experiences a vibration profile with an equivalent energy distribution and random nature.
This provides the highest possible realism and is essential for validating components against transient shocks and non-stationary vibrations.
Therefore, the modern approach often involves standards that provide foundational requirements, which are refined or replaced by mission-specific and in-field data to achieve a more accurate test.

### 1.2.2 The Qualification Lifecycle in Aerospace

In the aerospace sector, environmental qualification is a rigorously structured process deeply integrated into a spacecraft's development lifecycle. The testing philosophy follows a logical progression from the validation of individual components and subsystems to the full system-level qualification of the integrated satellite [4].

This process can be mapped (Figure 1.5 source [3]) onto the primary milestones of a space program:

1. **Development Phase:** Individual components and subsystems are subjected to qualification tests to meet their specified requirements.
2. **Integration Phase:** As the spacecraft is assembled, the integrated subsystems undergo further testing to validate their performance in a coupled configuration.
3. **Qualification Phase:** The fully assembled spacecraft is subjected to a final, comprehensive environmental test campaign.

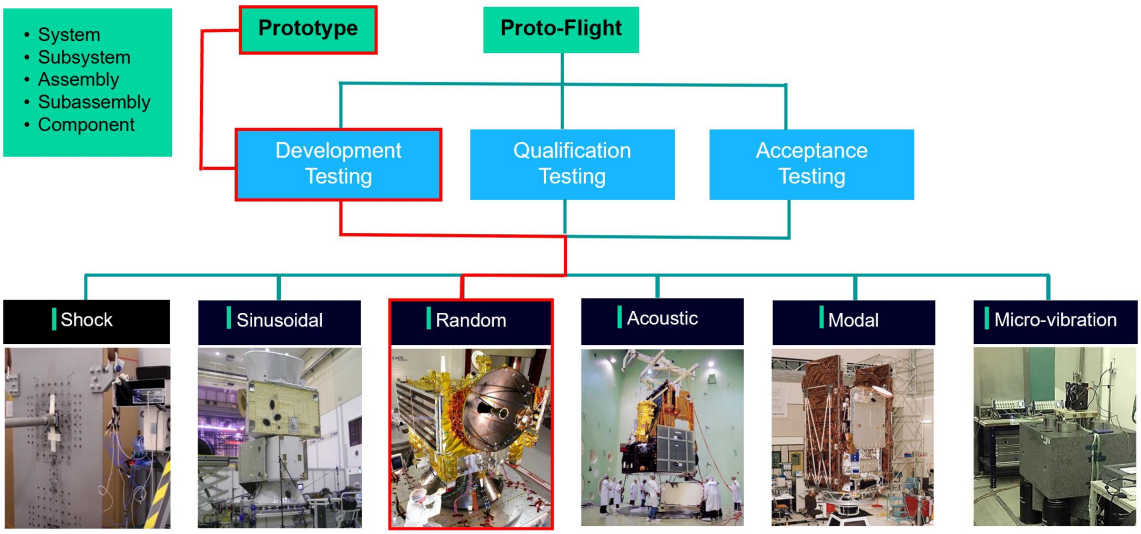


**Figure 1.5:** Qualification Scheme.

The **Prototype model** utilizes a dedicated, non-flight test article that may be tested to destruction to identify ultimate design margins and the **Proto-Flight model**.
In the Proto-Flight approach, the actual flight-ready hardware undergoes a consolidated qualification and acceptance test campaign, typically to slightly lower levels than a prototype to avoid introducing unnecessary fatigue damage.

### 1.2.3 Principles of Closed-Loop Vibration Control Testing

The primary objective of this system is to accurately and safely reproduce a specified dynamic environment by imposing a Device Under Test (**DUT**) to follow a predefined reference profile. This is achieved through a real-time feedback mechanism that continuously adjusts the system's output, defining a control loop (source [6]).

#### 1.2.3.1 Architecture of Vibration Control Systems

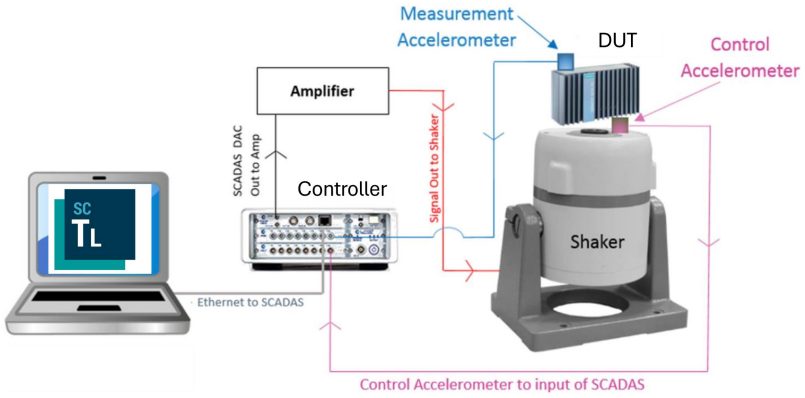


**Figure 1.6:** Control test scheme.

**The Controller:** It hosts the control software, which performs several critical functions, as shown by the scheme in Figure 1.6 (source [7]). It generates the initial drive signal, acquires and processes high-frequency data from the system's sensors, performs a real-time comparison of the measured response against the reference profile, and executes the complex control algorithms necessary to update the drive signal and ensure test stability and accuracy.

**The Excitation System:** Composed of a power amplifier and a shaker, this subsystem is the actuator that imparts mechanical motion to the DUT. The amplifier supplies the high-power signal to drive the shaker armature to the specified acceleration levels across the entire frequency range.

**Device Under Test:** The DUT is connected to the shaker with a fixture that provides the mechanical interface. The fixture must exhibit sufficient stiffness and be free of dynamic resonances within the test's frequency range.

**Instrumentation:** Accelerometers serve as the sensory feedback for the control loop. A distinction is made between two types of channels:

- **Control Channels:** One or more sensors located directly at the fixture or DUT interface. Their signal provides the primary feedback that the controller uses to close the loop and adjust the drive signal.
- **Measurement Channels:** Additional sensors placed at various points of interest on the DUT. While not used for direct control, their responses are continuously monitored to ensure that localized vibration levels remain within safe, predefined limits.

#### 1.2.3.2 Safety Mechanisms and Protection Protocols in Vibration Testing

Given that qualification testing often pushes a DUT to the limits of its design envelope, robust safety mechanisms are a non-negotiable control system component. Their primary function is to protect the high-value test article from damage due to unforeseen dynamic responses or control instabilities. The user defines these protection thresholds.

**Alarm Limits:** Functioning as a precautionary warning boundary, these are typically set as a tolerance band (e.g., ±3 dB) around the reference profile. If a measured response on any channel exceeds this limit, the system notifies the operator but typically continues the test, serving as an early indication of deviation from the expected behavior.

**Abort Limits:** Representing absolute safety boundaries, these are set at a wider tolerance (e.g., ±6 dB or more). If any channel's response breaches an abort limit, the control system executes the shaker's immediate but controlled shutdown. This action is designed to be a *fail-safe*, preventing catastrophic damage from an uncontrolled dynamic excursion.

#### 1.2.3.3 Overview of Qualification and Investigative Testing Regimens

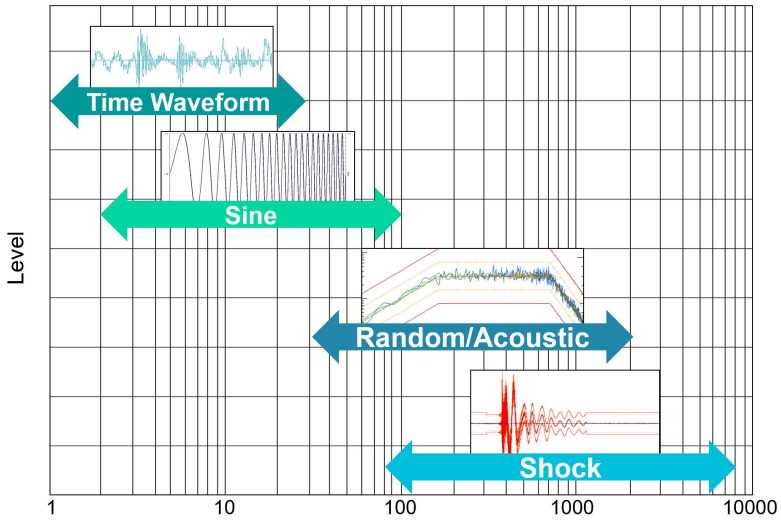


**Figure 1.7:** Tests spectrum Bandwidth (Figure extracted from [8]).

These methodologies (Figure 1.7) can be broadly categorized based on their primary engineering objective: **Qualification Tests**, which are designed to verify the survivability of a test article against a specified load, and **Investigative Tests**, which are employed to characterize its intrinsic dynamic properties.

**Sinusoidal Test:** This deterministic method subjects a test article to a sinusoidal excitation sweeping across a range of frequencies. It helps precisely identify structural resonances and qualify hardware against sustained, discrete-frequency loads typical of rotating machinery.

**Random Test:** This stochastic methodology is the standard for simulating complex, broadband dynamic environments like rocket launches or ground transport. The principle is to excite the article with a random signal whose statistical properties match a predefined PSD profile.

**Shock Test:** This procedure assesses the survivability of a component against high-amplitude, short-duration transient events. The methodology involves reproducing a specified time-domain shock pulse on an electrodynamic shaker, quantified via its **Shock Response Spectrum (SRS)**.

**Acoustic Qualification Test:** This test simulates the intense acoustic pressure field experienced within a launch vehicle's fairing. It is typically performed in a **reverberant chamber** or via **Direct Field Acoustic Noise (DFAN)** using a loudspeaker array (Figure 1.8).

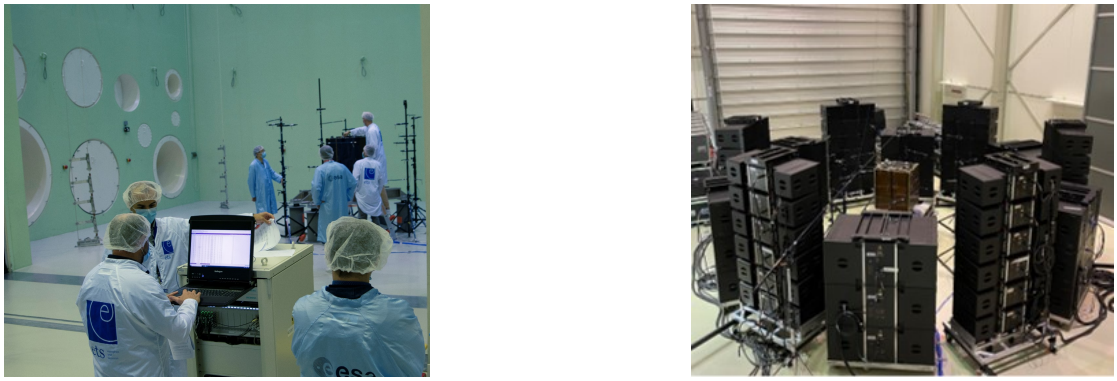

**Figure 1.8:** Reverberant chamber on the left vs loudspeaker array for a DFAN test on the right (source [4]).

#### 1.2.3.4 The MIMO Random Control Paradigm

A Multi-Input Multi-Output (MIMO) vibration control test overcomes the limitations of single-axis testing by applying simultaneous, controlled excitation from multiple shaker inputs (source [9]). The core challenge is calculating the precise shaker drive signals required to achieve a desired, complex response at multiple control points on the structure. This moves the problem from a simple scalar control loop to a complex matrix formulation in the frequency domain.
The target for a MIMO random test is not a simple PSD curve, but a full **Spectral Density Matrix (SDM)**, denoted as $\mathbf{S_{rr}}$. This matrix completely defines the target vibration environment at every frequency:

- **Diagonal Elements (PSDs):** The terms on the main diagonal ($\mathbf{S_{rr}}(i,i)$) are the PSDs, which define the average power of the vibration at each control point $i$.
- **Off-Diagonal Elements (CSDs):** The off-diagonal terms ($\mathbf{S_{rr}}(i,j)$) are the Cross-Spectral Densities (CSDs). These complex-valued functions encode two critical pieces of information about the relationship between any two control points $i$ and $j$:

- **Coherence:** The magnitude of the CSD, when normalized, gives the coherence. A value between 0 and 1 describes how linearly related the two signals are at that frequency. A coherence of 1 means the motion at one point is perfectly predictable from the motion at the other; a coherence of 0 means they are completely independent.
- **Phase:** The angle of the CSD defines the phase relationship. For example, a phase of 0° means the points move together (in-phase), while a phase of 180° means they move in perfect opposition.

The relationship between the shaker inputs (drive) and the system responses (controls) is governed by the system's **Frequency Response Function (FRF) matrix**, **H**. In the power domain, this fundamental input-output relationship is expressed as:

$$\mathbf{S_{yy}} = \mathbf{H}\,\mathbf{S_{xx}}\,\mathbf{H}^{\dagger}$$

where $\mathbf{S_{yy}}$ is the resulting output SDM at the control points, $\mathbf{S_{xx}}$ is the input SDM of the shaker drive signals, and $\mathbf{H}^{\dagger}$ is the Hermitian transpose (conjugate transpose) of the FRF matrix. The control task is to solve the **inverse problem** by setting $\mathbf{S_{yy}} = \mathbf{S_{rr}}$ and solving for $\mathbf{S_{xx}}$, we get:

$$\mathbf{S_{xx}} = \mathbf{H}^{+}\,\mathbf{S_{rr}}\,(\mathbf{H}^{\dagger})^{+}$$

where $\mathbf{H}^{+}$ is the **pseudo-inverse** of the FRF matrix. The controller must compute this matrix equation for every frequency line of the test, deriving the necessary power and cross-couplings for the drive signals to reproduce the target SDM on the structure accurately. This computationally demanding process forms the core of the MIMO closed-loop control algorithm. Coherence and phase determine whether points move together (high coherence, 0°), in opposition (high coherence, 180°), or independently (low coherence).

# Chapter 2

# Video Motion Magnification for Modal Analysis

## 2.1 Introduction to Structural Dynamics and Optical Methods

A comprehensive understanding of the dynamic behaviour of structures is paramount in engineering, particularly within the aerospace sector, to ensure operational safety and optimal performance.
Experimental Modal Analysis constitutes a foundational approach for identifying the intrinsic dynamic properties of a structure, including its natural frequencies, characteristic mode shapes, and damping ratios. These parameters are of critical importance for the validation of Finite Element Models (FEMs) and for applications in Structural Health Monitoring.
However, conventional experimental setups (Figure 2.1), which rely on contact sensors such as accelerometers or strain gauges, present several inherent challenges: complex installation procedures, mass-loading effects that can alter the system's natural dynamics, and pointwise measurements that risk overlooking distributed structural responses.
Research has increasingly gravitated towards **non-contact optical techniques** to overcome these limitations.
Laser Doppler Vibrometry facilitates high-precision point measurements, while DIC provides full-field displacement and strain data.
DIC, nevertheless, typically necessitates surface preparation (e.g., speckle patterns as depicted in Figure 2.2) and generates vast volumes of data that demand extensive post-processing.
This chapter introduces an alternative non-contact optical methodology: Video Motion Magnification, developed at MIT [10].
VMM amplifies imperceptible structural motions, rendering them visible and interpretable for qualitative modal analysis (source [11]). This work extends phase-based magnification techniques by employing Complex Steerable Pyramids (CSPs) to extract phase information, thereby facilitating the visualisation of Operational Deflection Shapes (ODS).

**Figure 2.1:** Accelerometer Setup (source [12]).

**Figure 2.2:** Image-Based Setup (source [13]).

## 2.2 Video Motion Magnification

This chapter delineates the entire workflow utilised for the VMM process, with the primary objective of applying a motion magnification for modal analysis. The overall process is schematised in Figure 2.3. Starting with an image sequence, the frequency spectrum and the PSD can be computed to identify the structure's resonance frequencies. For each of these identified frequencies, an optimal magnification factor is estimated, considering the algorithm's inherent limitations. Subsequently, the motion associated with the resonant frequency is amplified. The output is a video animation, where the magnified image sequence explicitly displays the ODS of the structure.

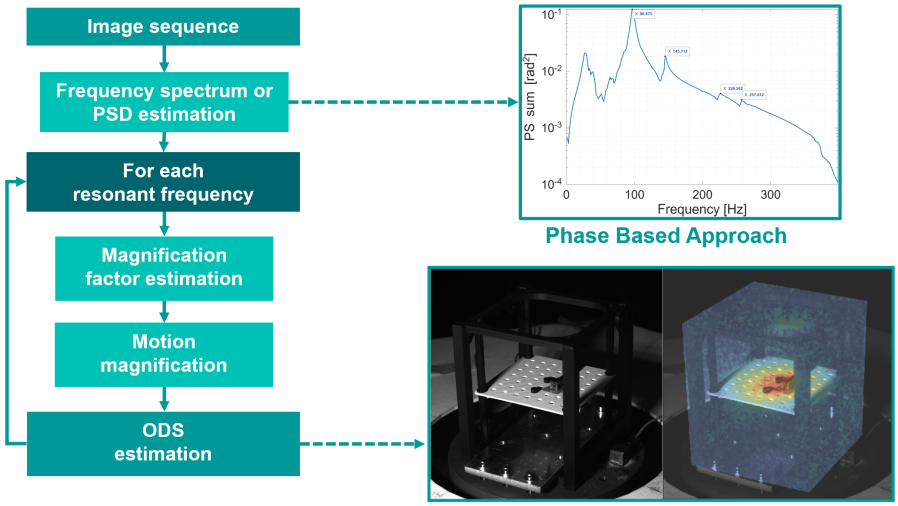


**Figure 2.3:** From the image sequence to the ODS video animation.

### 2.2.1 Motion magnification workflow

Both motion magnification and frequency spectrum estimation rely on local phase variations. These variations are obtained through Complex Steerable Pyramids, a richer decomposition method that utilises frequency and orientation, as shown in Figure 2.4. Initially, the

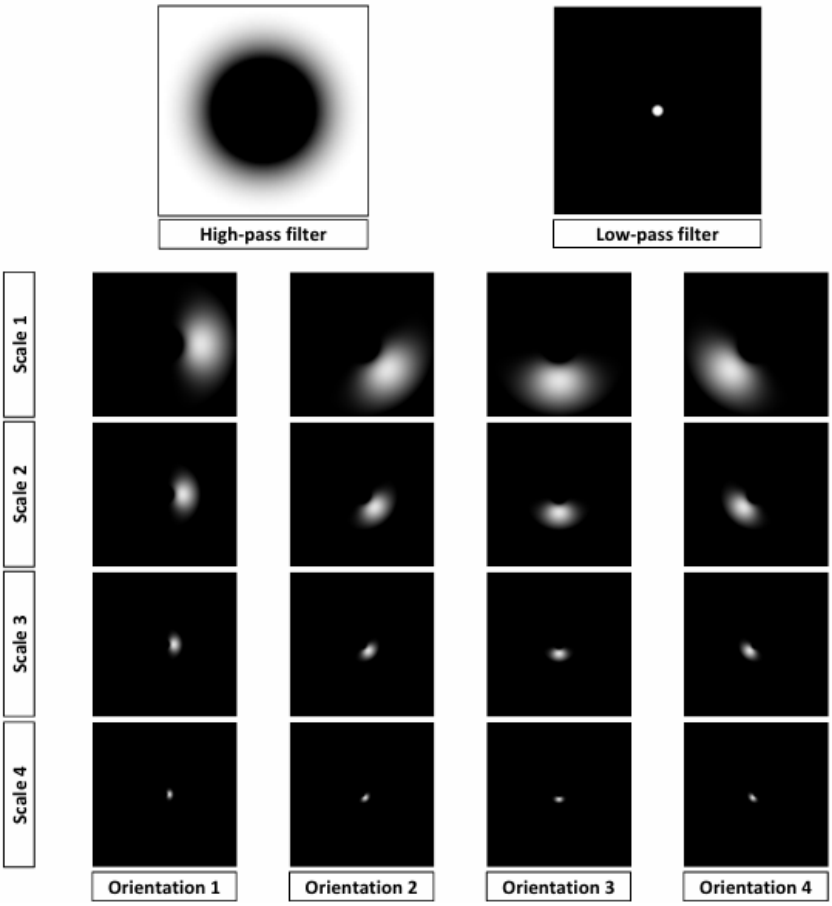


**Figure 2.4:** Sterable-Pyramid filter decomposition (source [14]).

magnification process, employed to extract and amplify these phase variations, is presented. Following this, the phase information can be utilised to estimate the frequency spectrum of the structure.

### 2.2.2 Decomposition, magnification and reconstruction

To effectively extract local phase information, the use of the complex steerable pyramid is fundamental.
The application of the filter banks necessitates a convolution operation between the image and the filter (source [15]):

$$\mathbf{L}^i_{\theta,s} = \mathbf{I}^i * \mathbf{\Psi}_{\theta,s} = \mathbf{M}^i_{\theta,s} e^{i\mathbf{P}^i_{\theta,s}} \tag{2.1}$$

In the frequency domain, this convolution transforms into a product. Consequently, for each level of the pyramid, the filters are generated in the frequency domain and multiplied by the Fourier Transform of the image. Reverting to the spatial domain yields the complex representation of the image $\mathbf{L}^i_{\theta,s}$. Executing this procedure for every frame within the image sequence enables the computation of the local phase for each level and for each frame. The phase variation can be estimated by multiplying the complex image $\mathbf{L}^i_{\theta,s}$ by the complex conjugate of the reference frame $\tilde{\mathbf{L}}^*_{s,\theta}$ and subsequently dividing by the squared magnitude of the reference complex image:

$$\Delta L^i_{s,\theta} = \frac{\mathbf{L}^i_{\theta,s} \cdot \tilde{\mathbf{L}}^*_{\theta,s}}{\tilde{\mathbf{L}}^i_{\theta,s} \cdot \tilde{\mathbf{L}}^*_{\theta,s}} \tag{2.2}$$

and finally extracting the phase of the resulting complex number:

$$\Delta \mathbf{P}^i_{\theta,s} = \arg(\Delta \mathbf{L}^i_{\theta,s}) \tag{2.3}$$

This procedure facilitates the extraction of the phase variation $\Delta \mathbf{P}^i_{\theta,s}$.
The phase variation must be temporally filtered to isolate a particular frequency band using a Finite Impulse Response (FIR) filter to precisely magnify a specific movement, such as a mode shape. Subsequently, the filtered phase variation can be multiplied by a magnification factor $\alpha$ and then added back to the complex image of the pyramid level:

$$\mathbf{R}^i_{\theta,s} = \mathbf{L}^i_{\theta,s} e^{i\alpha \Delta \mathbf{P}^k_{\theta,s}} \tag{2.4}$$

For the reconstruction of the magnified image $I_M$, the magnified pyramid level $\mathbf{R}^k_{\theta,s}$ must be convolved again with the pyramid filter and summed with all other level components:

$$\mathbf{I}_M = 2 \sum_{\theta,s} \mathbf{R}^i_{\theta,s} * \mathbf{\Psi}_{\theta,s} \tag{2.5}$$

This entire operation can also be performed in the frequency domain. A summary of this process is shown in Figure 2.5 (shared by Lorenzo [14]).

However, when employing the motion magnification algorithm to enhance a structure's ODS, the objective is not to display the entire magnified temporal sequence. Instead, the focus is directed towards a single cycle of the vibration. The algorithm can thus be slightly modified to accommodate this specific requirement. During the temporal filtering step, rather than applying a band-pass filter to the temporal signal, only a single sinusoid from the Discrete Fourier Transform (DFT) that corresponds to the mode shape's frequency is selected. Each pixel of the image is then animated by its respective sinusoid. In this scenario, rather than adhering to Equation 2.6, only the pyramid level of the reference image is utilised:

$$\mathbf{R}^i_{\theta,s} = \tilde{\mathbf{L}}^i_{\theta,s} e^{i\alpha \Delta \mathbf{P}^i_{\theta,s}} \tag{2.6}$$

where $\tilde{\mathbf{L}}^k_{\theta,s}$ represents the complex pyramid level of the reference frame, and $\Delta P^k_{\theta,s}$ is now a single sinusoid, no longer inherently tied to the test's original time step, thereby allowing for a desired time step.

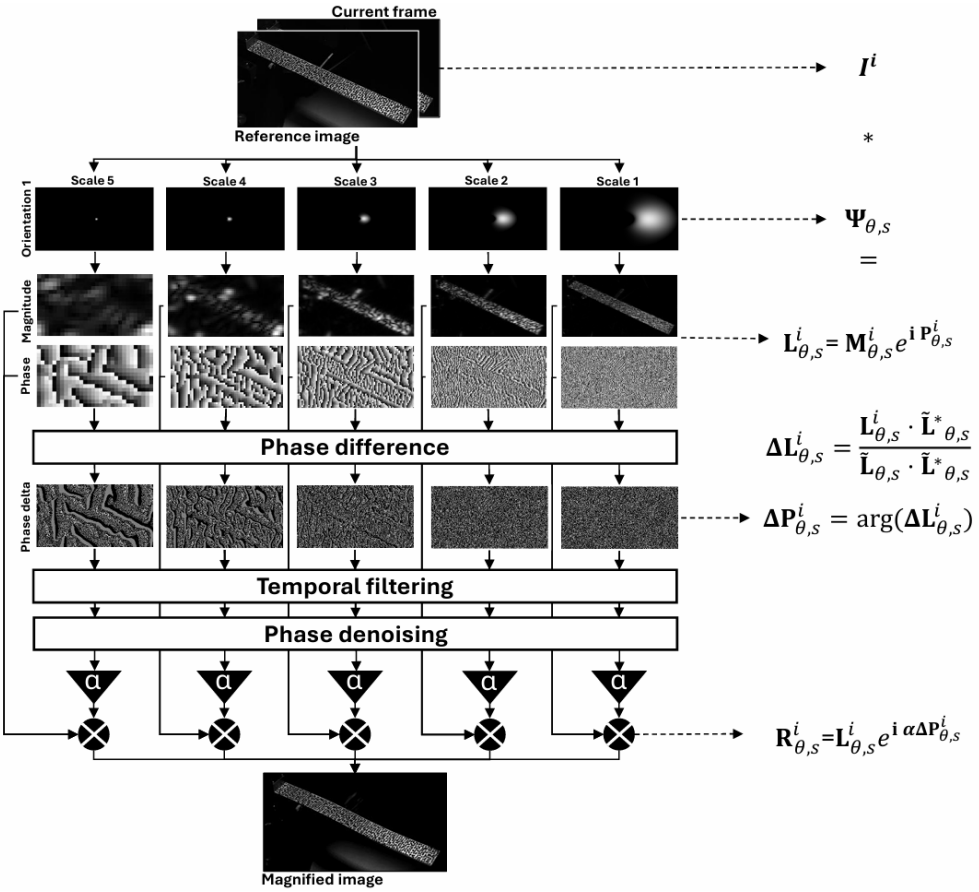


**Figure 2.5:** Video Motion Magnification workflow (source [14]).

### 2.2.3 Frequency spectrum and PSD estimation

Motion Magnification should be utilised to visualise mode shapes, based on the resonant frequency selected before the magnification process. Although a structure's frequencies can be determined through alternative means, extracting them directly from the image sequence proves more effective, as the frequency content derived from the video will be precisely that which is subsequently magnified by the algorithm. Since phase variation is intrinsically linked to motion, its time series, on a per-pixel basis, can be employed for frequency spectrum estimation. Each pixel can therefore be regarded as a displacement sensor, and the Fourier Transform of the time signal facilitates the calculation of the frequency spectrum:

$$\mathbf{\Phi}^k_s = \sum_{i=1}^{N} \Delta\mathbf{P}^i_{\theta,s} e^{-i2\pi\frac{(i-1)(k-1)}{N}} \tag{2.7}$$

Since a phase variation exists for each level, all these individual contributions must be summed and weighted by the magnitude of the sub-band level, given its correlation to the

noise level of the associated phase information:

$$\mathbf{\Phi}^k = \frac{\sum_{\theta,s} \mathbf{\Phi}^i_{\theta,s} \tilde{M}^2_{\theta,s}}{\sum_{\theta,s} \tilde{M}^2_{\theta,s}} \tag{2.8}$$

This particular step does not account for potential noise within the signal; hence, an averaging procedure in the frequency domain across a subset of pixels is necessary to yield a more accurate frequency spectrum. As the outcomes of these operations are localised to specific regions of the image, it is imperative to analyse multiple subsets across the structure to ensure that all mode shapes are adequately captured. Furthermore, because the frequency spectrum is derived from time-domain phase variation, straightforward signal processing techniques can be applied to mitigate issues such as spectral leakage. For this reason, the phase variation can be filtered using exponential or Hanning windows prior to calculating the Fourier Transform.
Once the frequency spectrum has been estimated for distinct regions across the structure, it becomes possible to estimate the Power Spectral Density matrix $G$, which contains both autopower and cross-power spectra. Starting from the Power Spectra matrix $S$, where each component of the matrix can be computed as:

$$S_{ab}(f) = \mathbf{\Phi}_a(f)\, \mathbf{\Phi}^*_b(f) \tag{2.9}$$

where $\mathbf{\Phi}_a(f)$ denotes the Fourier Transform of subset $a$ and $\mathbf{\Phi}^*_b(f)$ represents the complex conjugate of the Fourier Transform of subset $b$. From this point, the PSD can be estimated by dividing by the frequency resolution:

$$\mathbf{G}_{ab}(f) = \frac{\mathbf{S}_{ab}(f)}{\Delta f} \tag{2.10}$$

where $\mathbf{G}$ is the PSD matrix.

### 2.2.4 Optimise the magnification factor

In a vibrating structure, an increase in frequency is typically paired with a decrease in the amplitude of displacements. In this context, since phase information is directly proportional to displacement, phase variations similarly diminish at higher frequencies. Consequently, applying a uniform magnification factor across all mode shapes is not feasible. For simplicity in determining the magnification factor, it is estimated based on the boundary limits of phase-based motion magnification, as comprehensively discussed in [16, 17]. These bounds are intrinsically linked to the support of the filters; exceeding these limits would lead to artefacts in the reconstructed image.
Briefly, each pyramid filter possesses a confined spatial support due to the inherent requirement of isolating local phase information. Shifting image features by phase-shifting the complex pyramid filter causes them to move beyond this support. The greater the shift of these features, the more they become attenuated from within the filter window. Utilising an approximate analytical model of an image feature displaced by phase-shifting the localised

filter of the steerable pyramid, the magnified phase difference can be expressed as:

$$\Delta\phi = 2\pi\omega_0\delta(t) \tag{2.11}$$

where $\delta(t)$ denotes the shift in pixels, $\alpha$ is the magnification factor, and $\omega_0$ represents the peak frequency of the specific filter. From [16], a plausible limit to the magnified displacement can be defined as:

$$\alpha\delta(t) < \frac{1}{4\omega_0} \tag{2.12}$$

Thus, from Equation 2.11 and Equation 2.12, it is possible to derive that:

$$\alpha < \frac{\pi}{2\Delta\phi} \tag{2.13}$$

This relationship holds for octave decomposition. For sub-octave decompositions, such as half-octave and quarter-octave with $n = 2$ and $n = 4$ filters per octave, respectively, the extended form becomes:

$$\alpha < n\frac{\pi}{2\Delta\phi} \tag{2.14}$$

Employing the provided approximation, the maximum magnification factor for each frequency is estimated as follows. Initially, a Region of Interest (ROI) is defined on the structure. Within this ROI, the maximum magnification factor is calculated for each pixel. Subsequently, the ROI is divided into smaller subsets, and the average of the pixels within each subset is computed to account for the effects of phase noise. The minimum value derived from these averages is then selected to ensure that the magnification does not transgress its defined bounds at any point across the structure. This methodology prevents the magnification algorithm from generating artefacts in the final video output. However, in scenarios where distinct parts of the structure exhibit varying amplitudes of motion, the calculated magnification might prove insufficient to render the vibration visibly clear. In such instances, it may become necessary to deliberately exceed the computed limit by incrementally increasing the magnification factor to achieve the desired visual outcome.

# Chapter 3

# Thesis Workflow Overview: Virtual & Experimental Approach

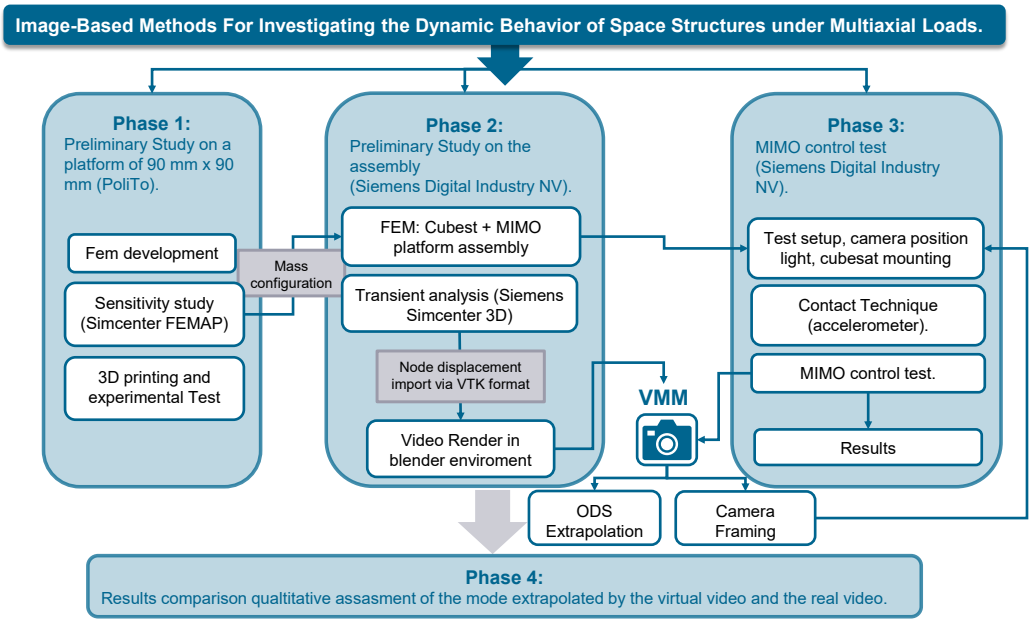


**Figure 3.1:** Steps of the Developed Workflow.

This thesis investigates the vibrational analysis of a CubeSat platform through a multi-stage workflow outlined in Figure 3.1. The process progresses from initial academic research to advanced industrial simulation and experimental validation. The preliminary university phase guided the design and mass configuration for subsequent development at Siemens Digital Industry NV.

**Phase 1: Preliminary Research (PoliTo).** The objective of this phase was to understand the fundamental vibrational behavior of a generic plate under varying mass placements. This understanding served as a critical foundation for optimizing mass configuration in the subsequent CubeSat model. Activities included investigating a generic square plate with variable mass placements, conducting a virtual analysis via Siemens Simcenter Femap to simulate its natural frequencies, and physically constructing and experimentally testing

the plate in a laboratory setting. The outcome of this phase provided crucial insights into how mass placement affects plate frequencies, directly informing the design choices for the CubeSat platform that would be developed later.

**Phase 2: Design and Simulation (Siemens Digital Industry NV).** The primary aim of this phase was to develop and simulate an optimized CubeSat platform, incorporating all the insights gained from Phase 1, and to prepare thoroughly for advanced experimental validation, particularly focusing on the VMM technique. This phase involved the development of a new CubeSat-specific plate geometry, which included integration with two specific masses, each weighing 2.5 grams, strategically positioned to target lower frequency ranges of interest indicated by the preliminary findings. The CubeSat assembly was then simulated on a 4-DOF platform using Simcenter 3D. A crucial preparatory step for the experimental phase was the pre-test virtual validation using VMM simulation. This process involved extracting the node's time-history data from the simulation to animate the vibrational behavior of the CubeSat in Blender, followed by virtual VMM testing on the Blender-rendered video. This virtual VMM step was instrumental in optimizing the real-world camera placement and enhancing the understanding of the VMM application prior to actual physical testing. The outcome of this phase was an optimized CubeSat platform design, virtual validation of the VMM methodology, and a refined strategy for the upcoming physical testing.

**Phase 3: Experimental Validation (Siemens Digital Industry NV).** This final phase focused on qualitatively assessing the CubeSat plate's vibrational behavior. The primary method employed was VMM, which involved extensive testing using video cameras to magnify and analyze subtle vibrations visually. This innovative approach was complemented by using accelerometers to gather comparative vibration data. Data from both VMM and accelerometers were rigorously analyzed. The overall outcome was the experimental confirmation of the simulation results from Phase 2, effectively demonstrating the efficacy and significant benefits of the VMM technique for structural dynamics analysis.

**Phase 4: Conclusions and Results Comparison.** This final phase included a comprehensive validation of the virtual data against the real-world test results, leading to definitive conclusions regarding the efficacy of the developed platform and the VMM approach. Additionally, it included discussions of optimization opportunities and suggestions for future work.

# Chapter 4

# FEM Model and Modal Analysis of a Test Plate

In this chapter, we aim to study the dynamic behavior of a 90 $x$ 90 mm plate, specifically how its modal characteristics change with the placement of a point mass. The plate was fabricated using a Bambu Lab A1 mini 3D printer and printed with FormFutura Tough PLA filament. We will begin by characterizing the material properties through tensile testing, followed by a detailed description of the FEM model and the subsequent modal analyses performed on both the unloaded and loaded plate.

## 4.1 Material characterization

To carry out preliminary analyses, the Young's modulus values of the material used to produce the plate on which the tests would be conducted needed to be obtained. By researching typical values, it was found that the material properties of the component varied widely depending on the 3D printing process. A material characterization test was necessary to ensure the reliability of numerical analyses. The plate was made of PLA, a plastic material, because of its low stiffness and light weight, highlighting the modal shapes at lower frequencies. Young's modulus was determined through a tensile test involving applying a controlled axial load to a specimen while measuring its elongation.

### 4.1.1 Tensile Test Setup for PLA

The test was carried out on a 3D printed ASTM D638 Type I speciment (Figure 4.2). It was clamped into a universal testing machine (Figure 4.1), part of the laboratory equipment of the Department of Mechanical and Aerospace Engineering of Politecnico di Torino, that applies a steadily increasing tensile force.

During the test, both the applied force and the resulting elongation are recorded. These values are used to generate a stress-strain curve (Figure 4.3), from which Young's modulus is extracted as the slope of the initial linear region, corresponding to the elastic deformation zone. The machine was previously calibrated using defective specimens (discarded because of shrinkage and twisting phenomena) to become familiar with the equipment and determine

**Figure 4.1:** Universal testing machine.

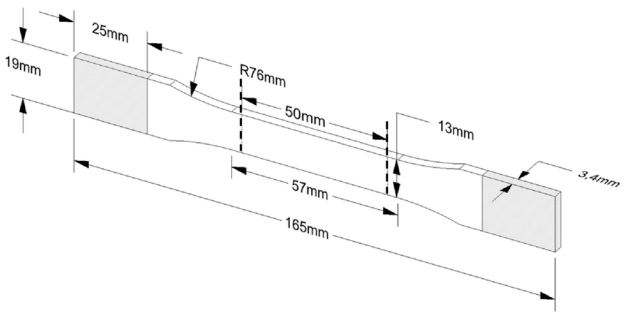


**Figure 4.2:** Type-I dimensions.

the appropriate displacement rate.
This step was crucial, as plastic materials are sensitive to the speed at which the load is applied. The tensile speed was set to 25 mm/min following these preliminary tests.

### 4.1.2 PLA Material Test Results

The final test was carried out on five specimens and produced the results shown in the Table 4.1.

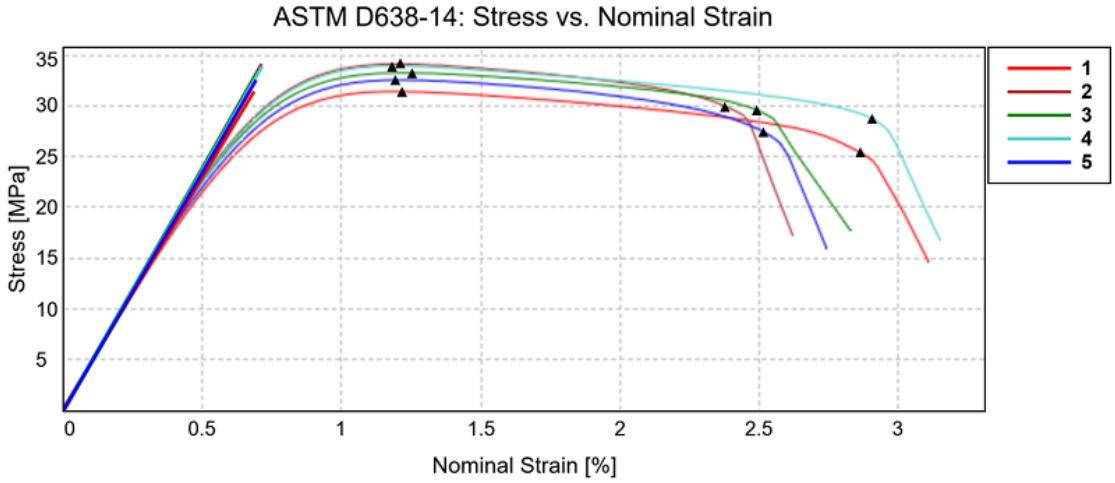


**Figure 4.3:** PLA test: stress vs elongation.

| Spec. | Width [mm] | Thickness [mm] | Young's Mod. [MPa] | Secant Mod. [MPa] | Tensile Str. [MPa] | Yield Str. [MPa] | % El. Yield [%] | % El. Break [%] | Nom. Strain [%] | Str. Break [MPa] |
|---|---|---|---|---|---|---|---|---|---|---|
| 1 | 13.00 | 3.200 | 1980 | 1910 | 31.4 | 31.4 | 2.80 | 6.59 | 2.87 | 25.4 |
| 2 | 13.00 | 3.200 | 2090 | 2010 | 34.1 | 34.1 | 2.78 | 5.47 | 2.38 | 29.9 |
| 3 | 13.00 | 3.200 | 2080 | 2000 | 33.2 | 33.2 | 2.89 | 5.73 | 2.49 | 29.6 |
| 4 | 13.00 | 3.200 | 2070 | 1990 | 33.9 | 33.9 | 2.71 | 6.68 | 2.90 | 28.7 |
| 5 | 13.00 | 3.200 | 2050 | 1950 | 32.5 | 32.5 | 2.74 | 5.79 | 2.52 | 27.4 |
| **Mean** | 13.00 | 3.200 | 2050 | 1970 | 33.0 | 33.0 | 2.79 | 6.05 | 2.63 | 28.2 |
| **S.D.** | 0.000 | 0.000 | 43.1 | 42.28 | 1.103 | 1.103 | 0.066 | 0.548 | 0.238 | 1.864 |

**Table 4.1:** Risultati prova ASTM D638-14

The specimens exhibit very similar behavior, with comparable breaking and yielding points observed in the tests. The analysis report confirms this: the root mean square deviation is slight, aligning with the graphical observations. Defining these material properties is the first step in creating a numerical model, which will then be used to make design considerations and assess the component's performance produced with the material of interest.
FEM analyses were carried out on the component to identify the frequencies at which the natural vibration phenomena of the CubeSat plate occur. SolidWorks was used for the 3D modeling, and the model was then imported into Simcenter FEMAP, where the modal analyses were performed.

## 4.2 Modal Analysis of the Unloaded Test Plate

The first step was to analyze the behavior of a simple square plate with a side length of 90 mm and a thickness of 1 mm. The plate has holes near its four corners with a diameter of 3.5 mm, through which it will later be attached to the satellite structure using spacers. The analysis was performed with a fixed constraint applied to the contour of the hole where the plate would be fastened to the structure.

### 4.2.1 Material Properties and FEM Model Simplification

The material was created using the properties obtained from the tensile test described in the previous chapter. It was applied to a Plate property, which defines the behavior of a two-dimensional element. This simplification of treating the object as a two-dimensional plate was adopted to reduce computation time, as a more detailed model would not have provided a significantly higher level of accuracy.

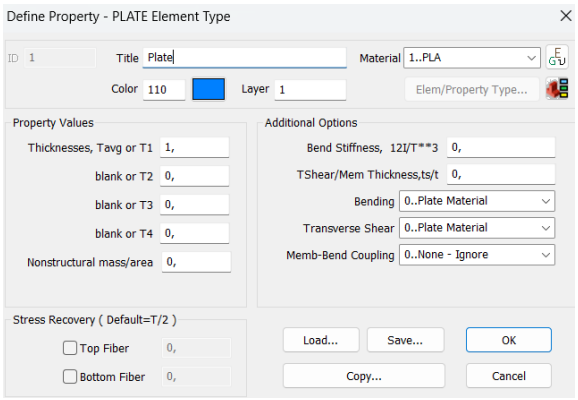


### 4.2.2 Mesh Generation and Refinement for Plate Model

The meshing operation was carried out with the aim of placing key nodes in specific locations Figure 4.4, to easily extract their displacements in a later comparison with experimental data. The plate was first simplified from a solid element to a surface. It was then further divided into smaller surfaces Figure 4.5.

The meshing operation was then carried out, considering the various surfaces, which required further refinement near the holes where the fixing constraints were applied. Simcenter FEMAP's mesh editing tools were used to insert elements along the curved lines, which were then refined in areas where the elements deviated from the ideal square shape required to avoid introducing errors into the analysis (Figure 4.6).

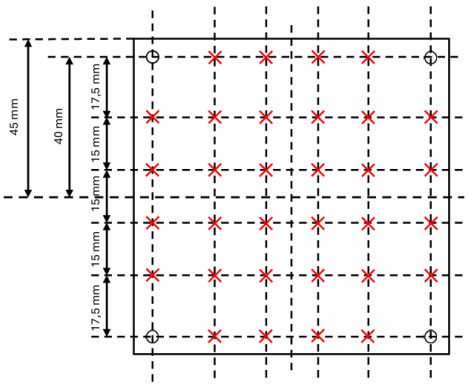


**Figure 4.4:** Evaluating point.

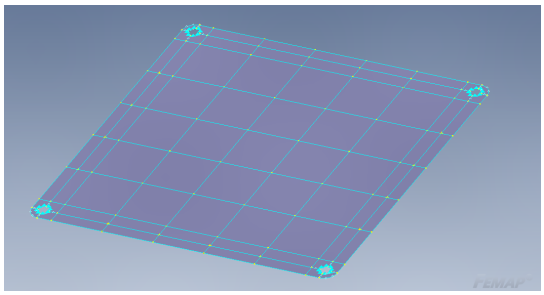

**Figure 4.5:** Geometry Subdivision obtained.

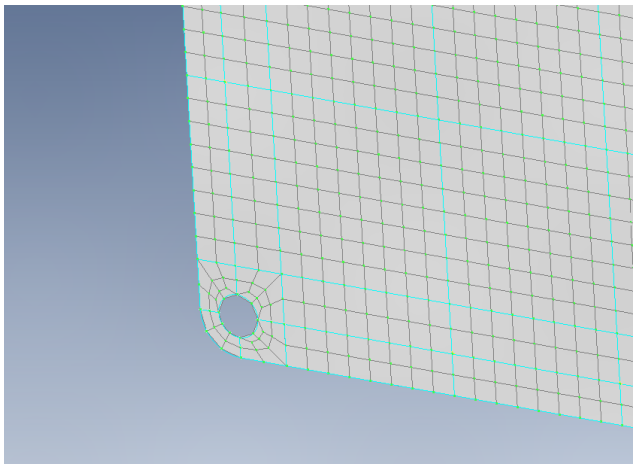

**Figure 4.6:** Hole mesh detail.

### 4.2.3 Identified Mode Shapes of the Unloaded Plate

Finally, a modal analysis was performed, which revealed the following behavior. The mode shapes along with their corresponding natural frequencies are shown in Figure 4.7.

Mode I

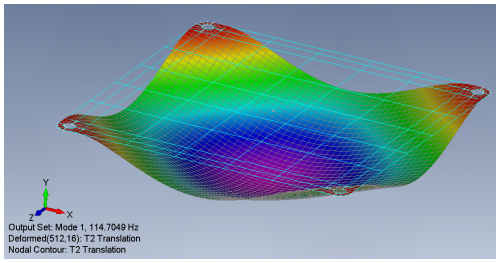


Mode II

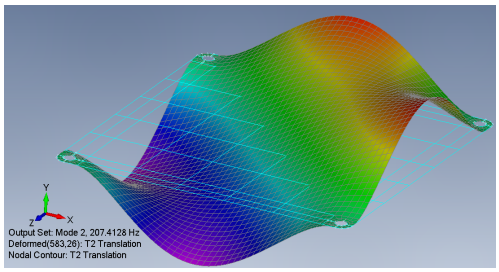

Mode III

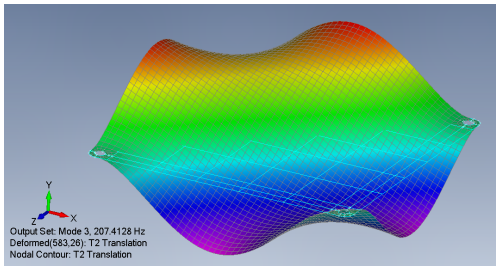


Mode IV

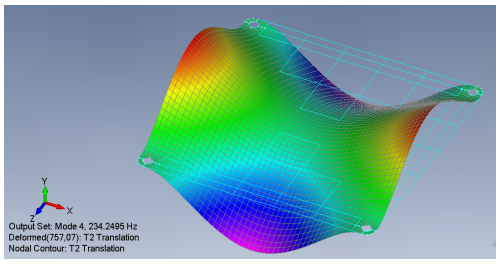


Mode V

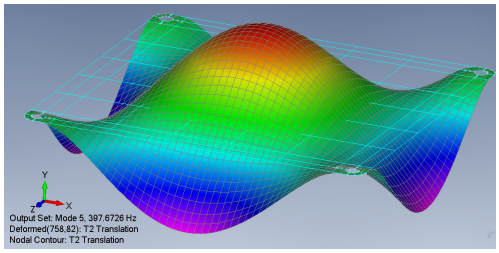


Mode VI

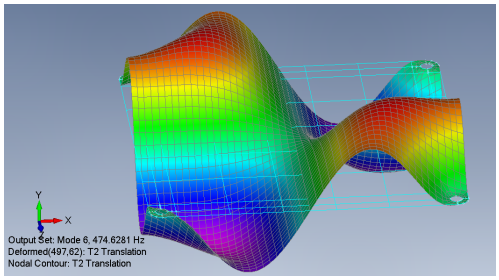


**Figure 4.7:** Plate ODS of interest.

## 4.3 Modal Analysis of the Test Plate with Concentrated Masses

Aiming to underst how the placement of masses influences the behavior of the plate, modal analyses were repeated for different values of concentrated mass at three different locations.

### 4.3.1 Load Application and Scenarios for Mass Influence

To simulate the presence of a mass, a concentrated mass element, defined as in Figure 4.8, was applied to a node of the mesh. This element was varied in absolute value within a range from 1 to 25 grams, with a finer variation in the initial loading steps.

Additional analyses were conducted by varying the location of the applied masses, following the placements shown in the Figure 4.9, to gain a deeper understanding of their effects.

## 4.4 Influence of Concentrated Mass on the Plate

The natural frequencies for each configuration were then extrapolated in a simple MATLAB code and displayed in the following Figure 4.10.

- **Point A:**

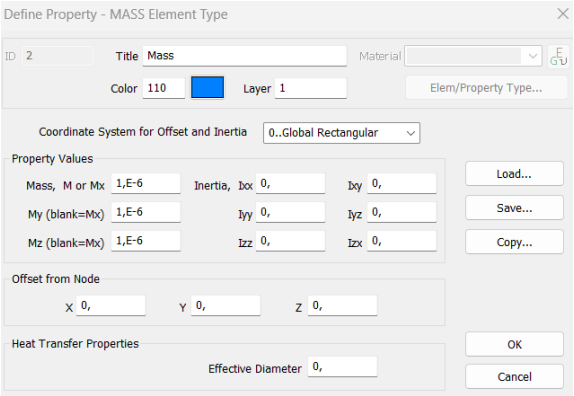


**Figure 4.8:** Concentrated Mass Definition.

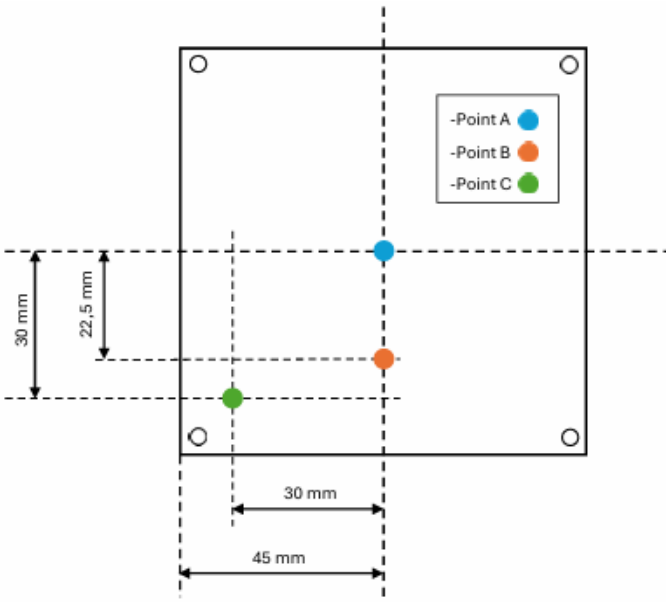


**Figure 4.9:** Loading points locations.

- Modes 1, 5, and to a lesser extent mode 10, are significantly influenced by the presence of the mass applied at the center.
- Modes 1 and 5 exhibit a more pronounced bulge at the center of the plate.
- All other vibration modes remain unaffected due to the high degree of symmetry of the plate.

- **Point B:**
  - The applied mass significantly influences modes 1, 2, 7, and 10.
  - Since this load point lies on an axis of symmetry of the plate, certain vibration modes are unaffected.
  - Mode 2 is very similar in shape to mode 3, but rotated 90 degrees.
  - Depending on the orientation of the plate, point B modifies the frequency of one of these two modes.

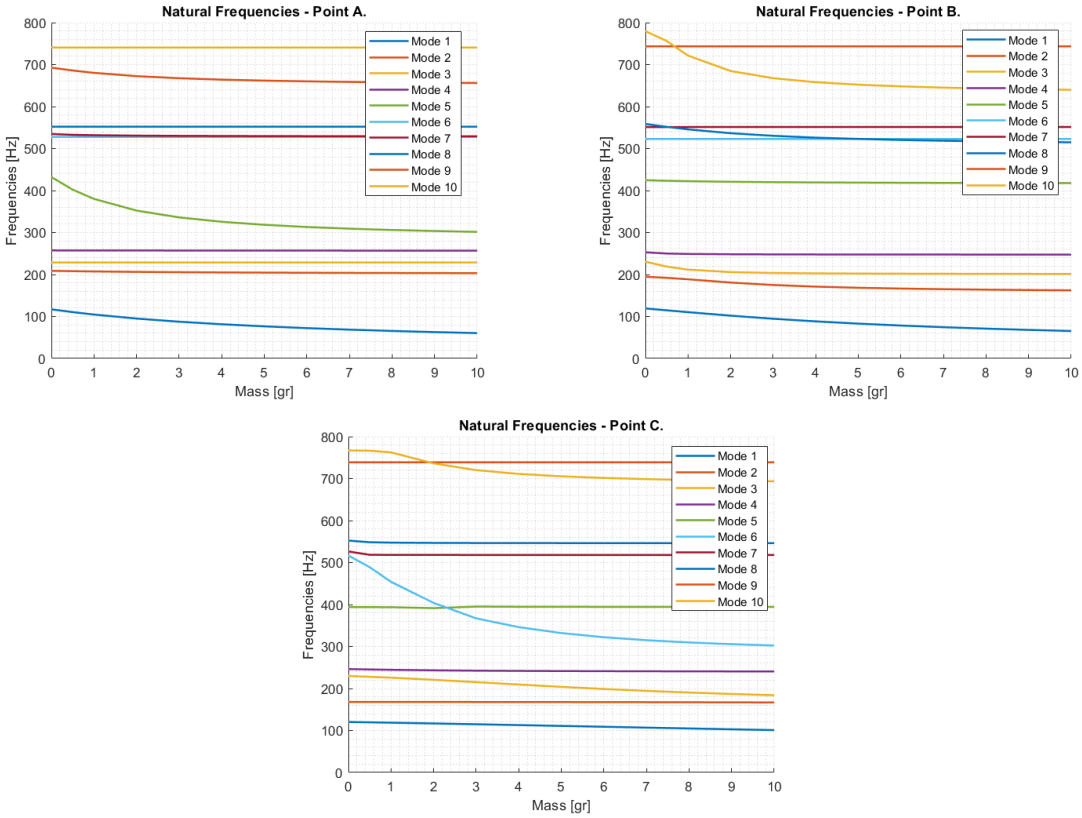


**Figure 4.10:** Mass influence over vibrational behaviour.

  - As the concentrated mass increases, mode 7 appears before mode 6.

- **Point C:**
  - The applied mass affects modes 1, 2, 5, 6, and 10.
  - This configuration differs because the mass is located along a diagonal and close to a boundary condition.
  - The reduction in mode 1 is less significant than when the mass is applied at point A.

# Chapter 5

# Experimental Validation of Test Plate Dynamics

In this chapter, the procedure followed to qualitatively estimate the behavior of the developed plate is described. The experimental campaign conducted at PoliTo tested the three different models presented previously. The primary objective was to verify whether the dynamic behavior of the 3D-printed plates aligns with computational predictions. Subsequently, the experimental results were retrieved and compared with the previously generated schemes based on numerically derived frequency-mass plots to quantitatively assess the models' accuracy. A simple setup was chosen to recreate a Z-direction oscillation in an open-loop test. The coherence was evaluated using an accelerometer placed near the fixture. A SoundCloud unit controlled the measurements of the two accelerometers, and an amplifier was connected between the computer and the shaker to amplify the signal.

## 5.1 Support Structure Design for Experimental Setup

The experimental setup required the design and fabrication of a custom mounting fixture. The shaker's actuator provides a central mounting point, whereas the plate's design specifies constraints at its four corners to replicate its in-service condition within a CubeSat assembly. A dedicated support structure was designed to bridge this interface. A key design criterion was to make the support significantly more massive than the plate under test. This ensures that the support's natural frequencies are substantially higher than the frequency range of interest (0-500 Hz), thereby preventing dynamic coupling and resonance interference. The design was further optimized, incorporating features to mitigate thermal shrinkage and warping, to ensure dimensional accuracy. The defined final support structure provides a stable and reliable platform for the experiment.

## 5.2 Test Workbench Assembly and Instrumentation

The complete test workbench was assembled using the custom support and the available components. Spacers were employed to elevate the plate from the support surface, replicating the boundary conditions defined in the numerical models. The plate was secured using

screws, which were fastened into threaded inserts in the support structure, facilitating an easy assembly procedure. Screws and a variable number of nuts were utilized to simulate the effect of a variable concentrated mass. Dedicated plates for each loading configuration (Point A, B, and C) were 3D-printed. Tests were conducted at three distinct mass values to provide validation points for the numerical curves.

### 5.2.1 Excitation Signal Definition

The system was excited using a broadband signal to cover the frequency spectrum of interest. The objective was to provide sufficient energy across all frequencies up to at least 500 Hz to ensure that all relevant structural modes of the plate were adequately excited and could then be identified in the response data.

### 5.2.2 Dual-Accelerometer Signal Acquisition

Signal acquisition was performed using a dual-accelerometer setup as shown in Figure 5.1.

- **Response Accelerometer:** The first accelerometer was mounted on the plate at a strategic location to avoid, as much as possible, placing it on the expected nodal lines of the mode shapes within the excited frequency bandwidth.
- **Input Accelerometer:** The second accelerometer was positioned near the shaker's actuator on the support structure to record a clean input excitation signal. This measurement is crucial to validate the reliability of the test through the coherence estimation.

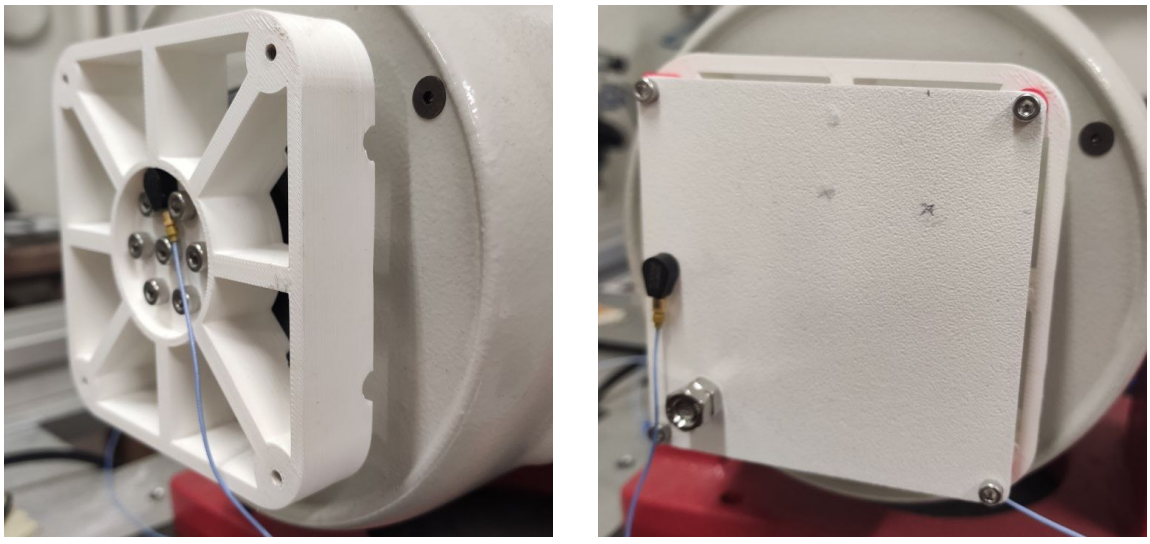

**Figure 5.1:** Accelerometers position within the setup configuration.

To ensure the consistency of the results for each loading condition, at least three repeated measurements were performed. The recorded time-domain signals were visually inspected to identify anomalies and statistically analyzed to categorize their amplitude and variability,

allowing for a more objective comparison between signals. This process was essential to confirm the similarity between repeated runs before proceeding to data analysis.

## 5.3 Experimental Data Analysis and Results

The time-domain signals acquired were subjected to post-processing utilising a MATLAB script. This script extract the acceleration measurement (from the accelerometer placed on the plate) and the corresponding coherence with the signal recorded from the accelerometer strategically positioned on the fixture, as provided by the SoundCloud device. Subsequently, the analytical procedure involved computing the FRF from these processed time-domain data, followed by applying the modalfit function to identify modal parameters.

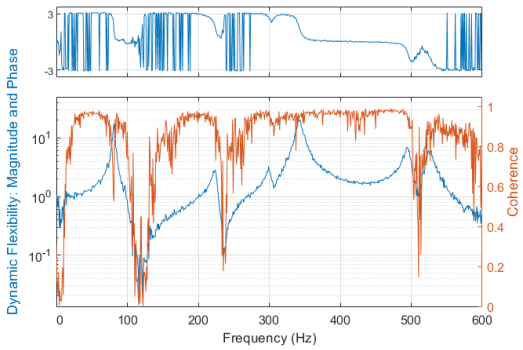


Signal and coherence in the frequency domain.

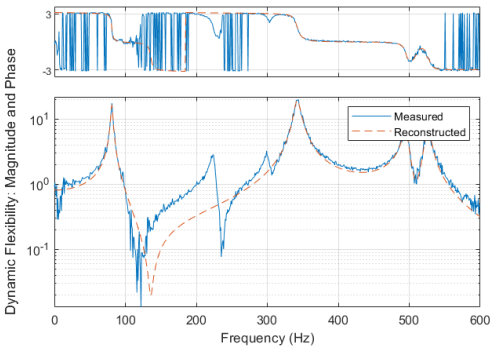


Peaks highlighted using the `modalfit` function.

**Figure 5.2:** Test Plate A, mass 6.5 gr.

Based on the results of the numerical modal analysis, several dominant vibration modes were expected to be clearly identifiable within the investigated frequency range. However, the experimental FRFs displayed limited coherence and irregular peak definitions, as shown in Figure 5.2. Although the modalfit function successfully identified some resonance peaks, it failed to accurately capture the overall modal trend, leading to an incomplete or distorted representation of the system's dynamic behavior. As a result, only a subset of the natural frequencies predicted by the numerical model was correctly detected, while other expected modes were either shifted in frequency or not recognized at all. Consequently, we observed a partial overall correspondence between experimental and numerical results, further illustrated by the comparisons in Figures 5.3. While a perfect match between these two domains was not anticipated, a more consistent alignment of the modal distribution and relative peak amplitudes was expected.

Several experimental factors may explain these discrepancies. The use of a single measurement accelerometer configuration limited the ability to effectively capture all relevant vibration modes. This limitation became particularly evident when the sensor was positioned near the nodal regions of specific mode shapes, where local displacements are minimal, resulting in a deteriorated signal-to-noise ratio. Moreover, non-ideal sensor mounting or

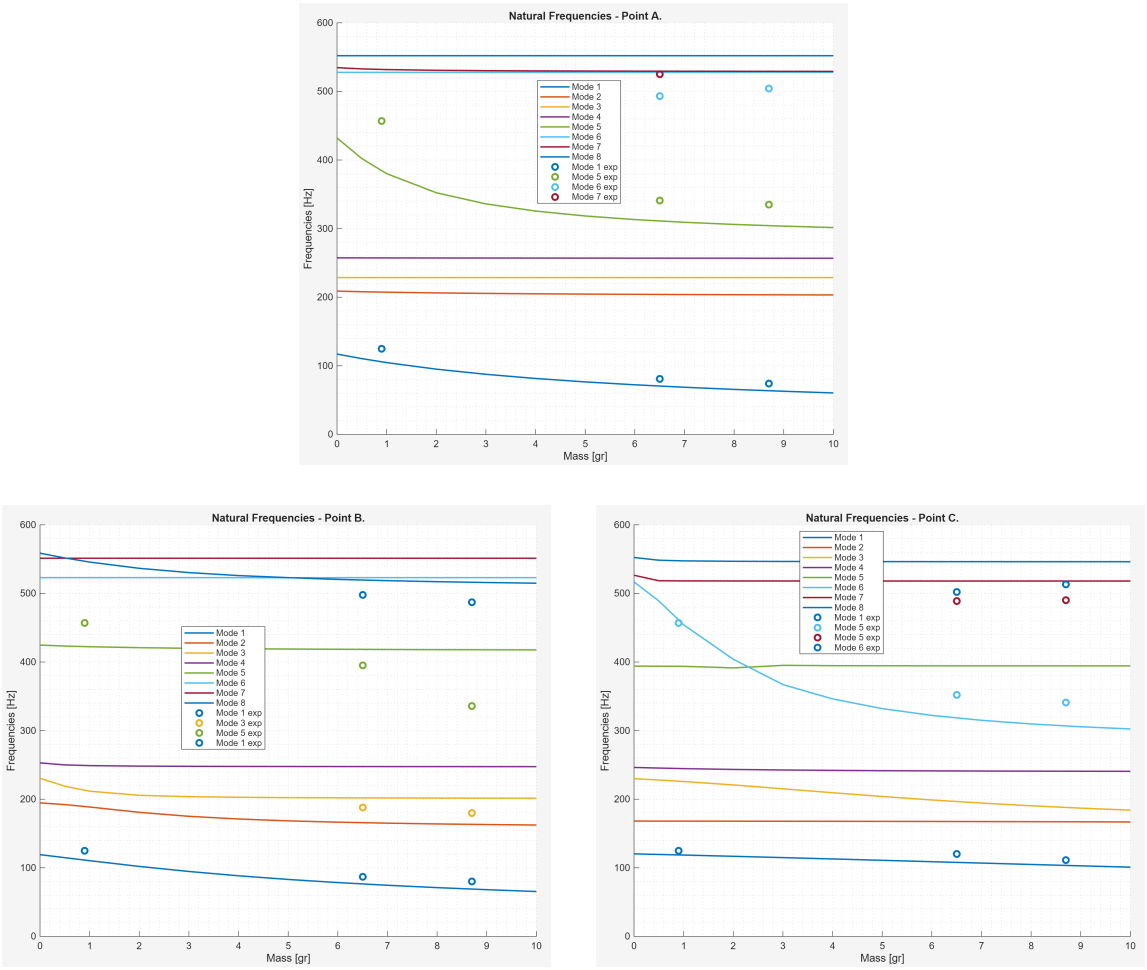


**Figure 5.3:** Overlay of the experimental data.

insufficient coupling stiffness may have introduced extra measurement noise or attenuated the response amplitude. These issues contributed to reduced data quality, preventing the modalfit algorithm from reconstructing the expected modal behavior.
Therefore, future tests should consider an expanded excitation and measurement setup, along with improved sensor mounting strategies, to enhance signal reliability and increase alignment with numerical predictions.

# Chapter 6

# Transient Analysis of the Integrated CubeSat Assembly

## 6.1 Introduction to Coupled System Analysis

This Chapter introduces a more complex system-level analysis, building upon the preliminary investigation of a single PLA plate subjected to Z-axis excitation, developed in the previous Chapter. The analytical framework, outlined in Chapter 1.2, combines conventional test methodologies for spacecraft under launch loads with a novel visual inspection technique. The workflow diagram in Figure 1.5 depicts the overall process for the qualitative characterization of the DUT. The central element of this study is a reliable computational model that integrates the CubeSat structure with the S.E.R.E.M.E. (4-DOF) MIMO platform (its functioning is described in 1.2.3.4) to investigate dynamic coupling phenomena. This Chapter delineates the transient dynamic analysis of the integrated CubeSat and S.E.R.E.M.E. platform assembly, performed in Siemens Simcenter 3D.
The analytical procedure was structured into three principal phases:

- development and validation of the FEM.
- pre-processing of the input excitation signal to align with test specifications
- configuration and execution of the final transient simulation

## 6.2 Finite Element Model Development for the Integrated Assembly

### 6.2.1 CubeSat Assembly Model Update

The analysis of the plate presented in Chapter 4 served as a valuable exercise. It provided a first practical application of testing guidelines and fostered familiarity with the behavior of a small-scale plate and the influence of distributed masses. However, that plate was developed without considering the CubeSat rig available at Siemens Industry Software NV, which had previously been characterized in the work of Samuele Montesion [18].

In its original configuration, this model featured five 2 mm thick plates made of PEEK, a significantly stiffer material.
Using the Siemens Simcenter 3D work tree, the assembly's .prt file was accessed, the five plates removed, and a 1 mm thick PLA plate was introduced in their place, as shown in Figure 6.1. This new component was positioned at the mid-plane of the CubeSat's internal volume. Since the rig geometry remained unchanged, the same mesh seed from the previous study was retained to ensure mesh continuity at the interface between the four support beams and the new plate. After updating the subsequent steps in the workflow, the model was successfully regenerated.

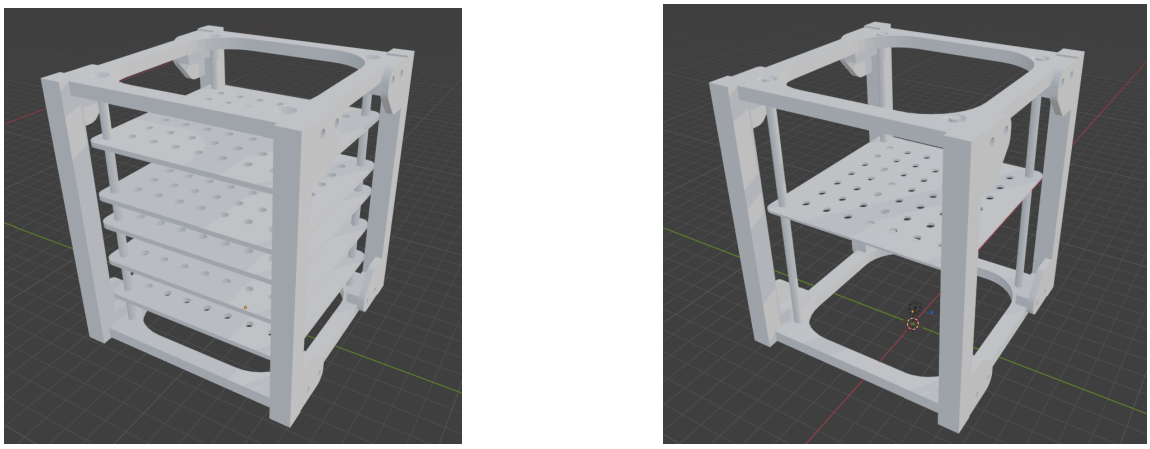

Original Assembly. Updated Assembly.

**Figure 6.1:** CubeSat Model Update.

### 6.2.2 Super Element Integration and Assembly Connection

The S.E.R.E.M.E. platform is represented computationally as a Nastran Superelement, a statically condensed mathematical representation that preserves the dynamic characteristics of the complex platform available in the Siemens facility. The structural interface between the DUT and the platform was established using rigid body elements (RBE2).
The master nodes of these elements were defined at the Superelement's attachment points, while the slave nodes were connected to the corresponding points on the bottom face of the CubeSat's vertical columns. This procedure was repeated three other times to ensure a rigid connection, simulating the boundary condition encountered during the actual mounting operation.

### 6.2.3 Modal Analysis of the Integrated Assembly

A modal analysis, utilizing the SOL 103 solution sequence in Siemens Simcenter 3D, was conducted to characterize the dynamic properties of the assembled model.
This step was necessary because the plate behavior extrapolated from previous work was unreliable, and the plate geometry was incompatible with the CubeSat structure. The new plate, featuring a different geometry, was designed for mounting on the rig. Several holes were incorporated in the design to apply various load conditions without manufacturing multiple specimens.

This analysis was fundamental for verifying the model's integrity and interpreting its

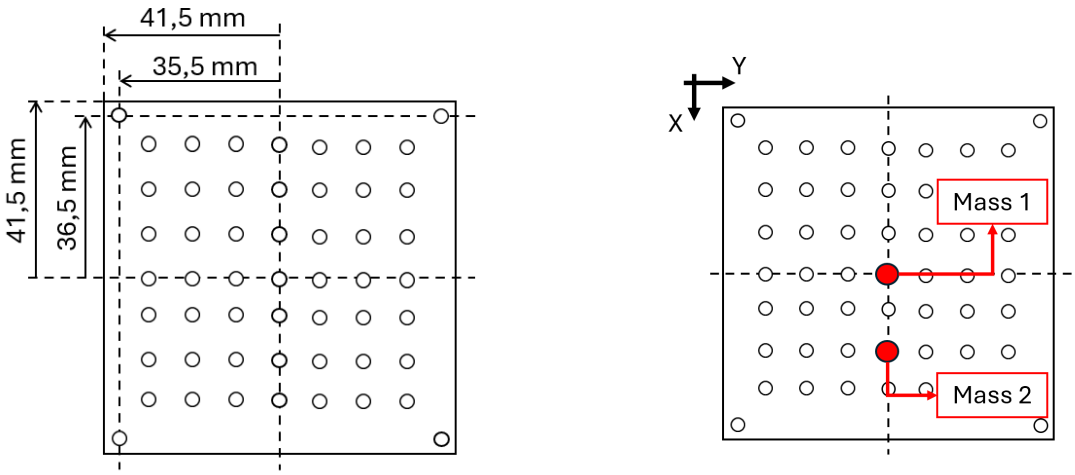


Plate geometry, holes 10 mm apart. Loading condition.

**Figure 6.2:** Plate geometry and loading scheme.

behavior before the transient simulation. Visual inspection of the mode shapes confirmed that the CubeSat and platform behaved as a coupled dynamic system.
As detailed in the previous Chapter, a single load condition consisting of two 2.5 g masses was investigated. The weights were loaded in the center hole and in a second hole, specified in Figure 6.2.
This configuration was chosen based on previous results to lower the system's natural frequencies, thereby enabling the evaluation of a greater number of mode shapes within the frequency range of interest.

To prevent the main body of the text from becoming overly burdened with figures, only the first two frequencies in Figure 6.3 are illustrated. Additional frequencies are detailed in Appendix A.
The modal analysis was performed on the assembly under fixed boundary conditions, where all six degrees of freedom were constrained at the four nodes corresponding to the shaker head connection points. This analysis identified the mode shapes with the most significant displacements. These dominant modes were subsequently saved (Table 6.1) for comparison with the transient analysis results.

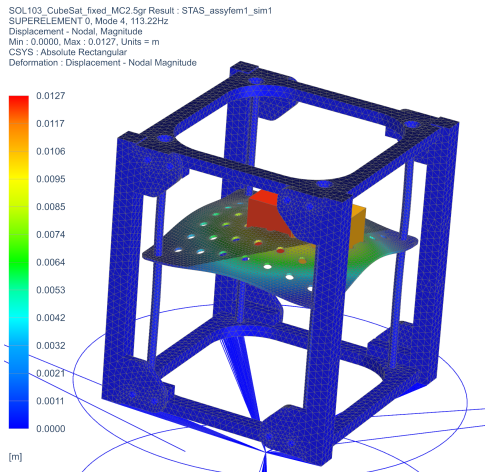


$f_1$, single bump.

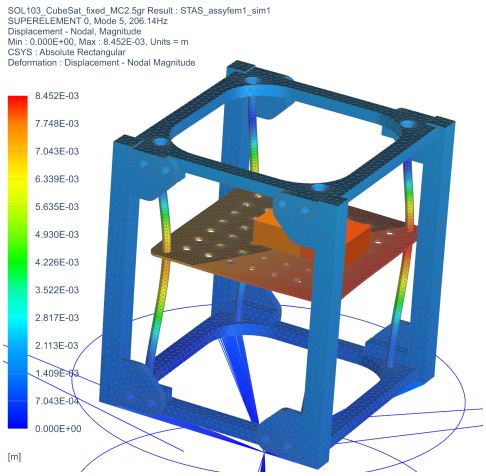


$f_2$, swing in Y.

**Figure 6.3:** First ODSs of interest.

| $f_1$ [Hz] | $f_2$ [Hz] | $f_3$ [Hz] | $f_4$ [Hz] | $f_5$ [Hz] | $f_6$ [Hz] | $f_7$ [Hz] | $f_8$ [Hz] | $f_9$ [Hz] | $f_{10}$ [Hz] |
|---|---|---|---|---|---|---|---|---|---|
| 113.22 | 206.14 | 210.60 | 252.56 | 297.37 | 309.25 | 337.34 | 365.30 | 335.61 | 457.97 |

**Table 6.1:** Frequencies of the modes of interest

## 6.3 Input Excitation Signal Definition

### 6.3.1 Signal Processing Workflow

Before its application in the FEM, the input excitation signals used for the MIMO random control test (performed with the S.E.R.E.E.M.E platform) underwent a dedicated analysis in MATLAB. This signal represents the real-life load profile (from manual [19]) of the VEGA C launcher (Figure 6.4), The objective was to obtain a set of transient input forces that were as representative as possible of the experimental test.
To ensure a computationally manageable transient analysis and facilitate subsequent data utilization, a 2-second segment of the signal was specifically extracted. This length was chosen to keep the transient analysis output within a reasonable data volume, typically 20 GB to 30 GB, which is crucial for efficient handling in downstream processes.


**Figure 6.4:** VEGA launcher (source [20]).

The workflow (Figure 6.5) consisted of the following sequential operations:

- **Initial Signal Acquisition:** The raw time-domain signal, extrapolated from the measurements at the force cells of the shaker connection, served as the initial input.
- **Low-Pass Filtering:** The signal's bandwidth was reduced to isolate the frequency

range of interest. This reduction was accomplished through the use of a low-pass square filter, which ensured a sharp frequency cutoff at 800 Hz and removed irrelevant high-frequency content.

- **Time Segmentation and Resampling :** The signal duration was truncated to a 2-second segment to optimize computational effort. Subsequently, the filtered signal was resampled to a lower sampling frequency of 800 Hz (subfactor of the original sampling frequency of 3200 Hz) as shown in Figure 6.6.
- **Verification:** Validation of the processed signal was performed by conducting a Fast Fourier Transform and a Power Spectral Density analysis (Figure 6.7). This step confirmed preserving the signal's primary energy and power characteristics within the target bandwidth.

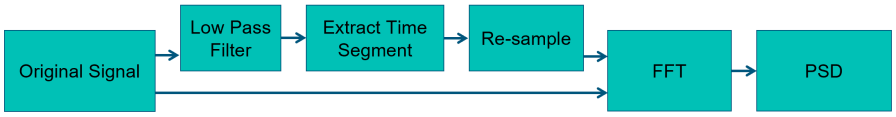


**Figure 6.5:** Workflow Scheme

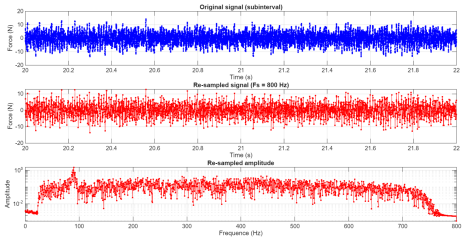


**Figure 6.6:** Resampled Signal

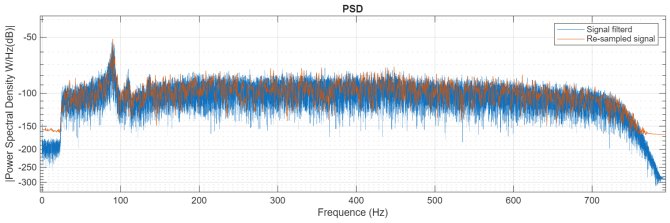


**Figure 6.7:** PSD comparison.

The final processed time-history was exported in a **.txt** format for subsequent import into Siemens Simcenter 3D as a time-dependent force table. This process was repeated on the signal, first band-limited to 800 Hz to isolate the dominant mode shapes, and then further reduced to 400 Hz.

## 6.4 Transient Dynamic Analysis Configuration

The processed 2-second time-history signal was applied as time-dependent forces at the shaker interface nodes on the Superelement, as shown in Figure 6.8.
The simulation was defined through the subcase definition with a time interval of 2 seconds and discretized into 1600 time steps, providing adequate temporal resolution to capture the system's dynamic response.
The primary output requested was the nodal displacement history, which was specified for export in the output request as a punch (**.pch**) file format. To reduce its weight, it was requested just for the cubesat assembly nodes through the 'Nodes Selection' option in the same window (some results displayed in Figure 6.9).

This operation produces a punch file of 20 GB, which would be crucial for the next steps of importing the geometry behaviour into the Blender environment.

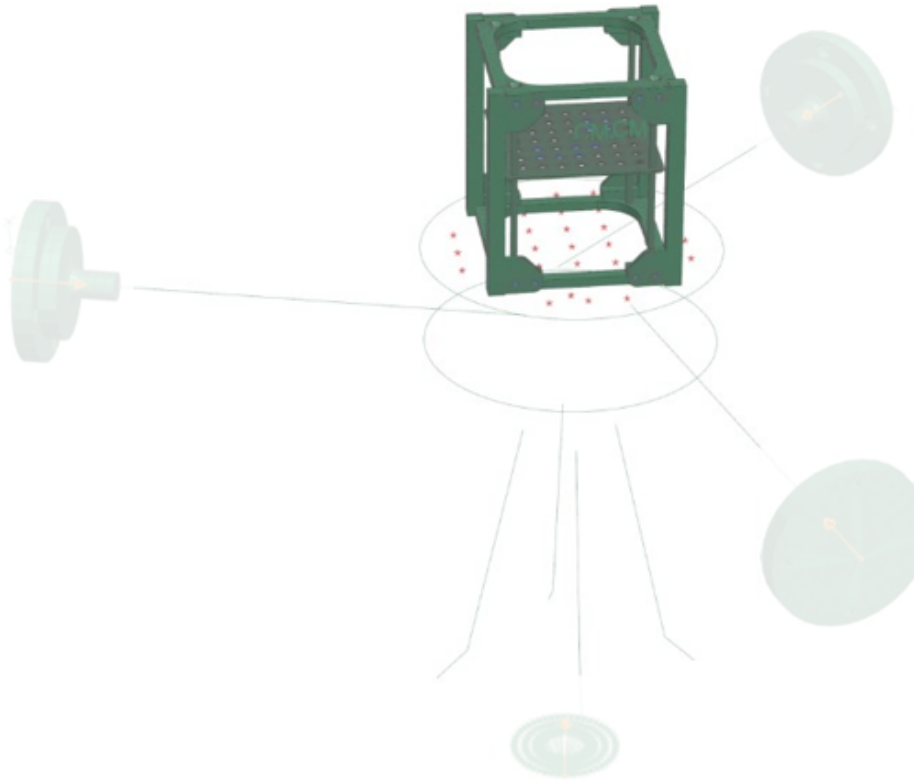

**Figure 6.8:** Assembly Load Condition.

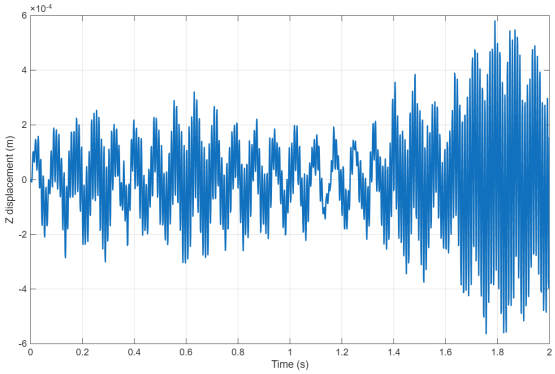


Displacement time history near Mass 1.

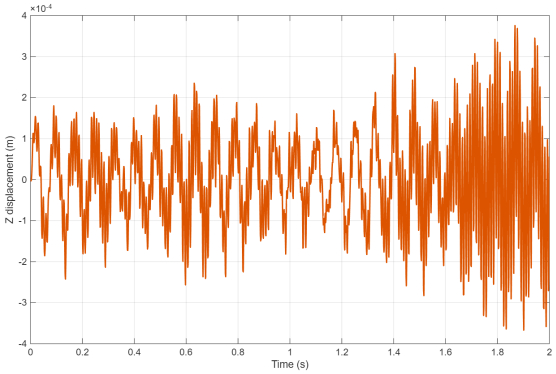


Displacement time history near Mass 2.

**Figure 6.9:** Time history displacement along Z direction, for two selected nodes (near Mass 1 and Mass 2, see Figure 6.2) of the assembly.

# Chapter 7

# Virtual Motion Video Generation and Pre-Experimental Analysis

## 7.1 Introduction to Virtual Test Campaign

After the transient analysis was successfully completed, the primary objective shifted to visualization and analysis of the simulated structural motion. The nodal displacement time-histories obtained from Siemens Simcenter 3D were leveraged to generate a high-fidelity virtual video. This video serves as a starting point for the virtual test campaign. This campaign aims to optimize the setup for the subsequent physical experiment, particularly regarding camera positioning and the selection of image analysis parameters. Thus, it aims to mitigate the iterative and time-consuming adjustments typically required during physical testing.

The workflow for this phase is centered around a toolchain integrating MATLAB for data processing and Blender, an open-source 3D computer graphics software, for visualization and video rendering.

## 7.2 VTK Data Conversion and Processing for Animation

### 7.2.1 The Role of the VTK File Format

The Visualization Toolkit (**VTK**) file format facilitates the link between the simulation results and the visualization environment. The **blenDIC** plugin for Blender [21], which is employed to animate the structure, is designed to import a sequence of **VTK** files, where each file represents the state of the model at a discrete time step. Consequently, a prerequisite was the development of a robust MATLAB script capable of converting Siemens Simcenter 3D outputs into this format. The script's core function is to parse the mesh and connectivity information from the **DAT** file and the nodal displacement time-histories from the **PCH** file, and subsequently reformat this data according to the **VTK** specification.

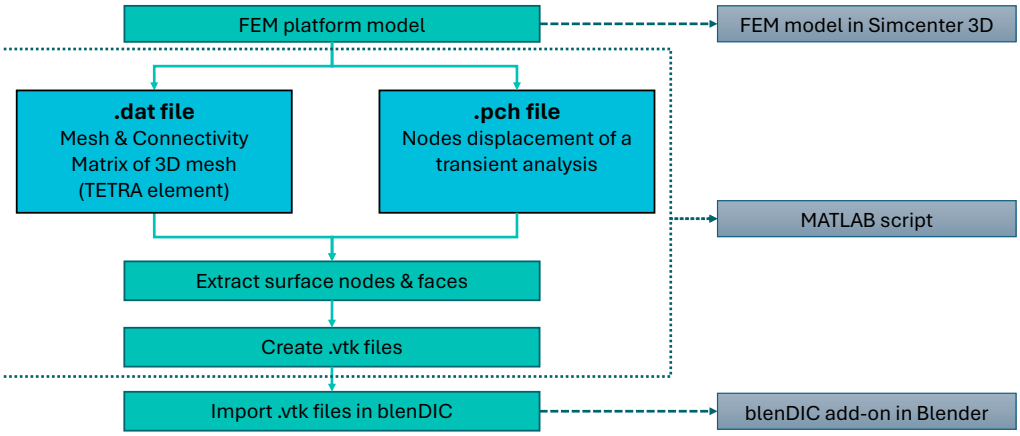


**Figure 7.1:** VTK Code scheme

### 7.2.2 Implementation Challenges and Solutions for VTK Conversion

This work builds upon a pre-existing code framework designed initially for models meshed with hexahedral elements. The current analysis, however, utilizes second-order tetrahedral elements (CTETRA10, with 10 nodes, Figure 7.3). This necessitated significant modifications to the MATLAB script.

A primary challenge was a compatibility limitation within the **blenDIC** plugin, which does not support second-order element definitions. To resolve this, the script was adapted to simplify the element topology by extracting only the first four corner nodes of each CTETRA10 element. This process effectively converts the mesh to a first-order representation (CTETRA4 Figure 7.2). While this simplification introduces a degree of approximation in the displacement field, the high mesh density is expected to minimize the loss of fidelity for visualization purposes.

A further significant challenge was the computational burden associated with processing

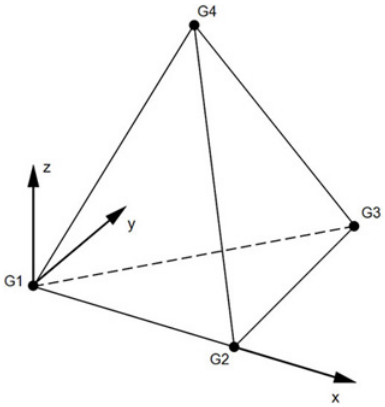


**Figure 7.2:** I order CTETRA.

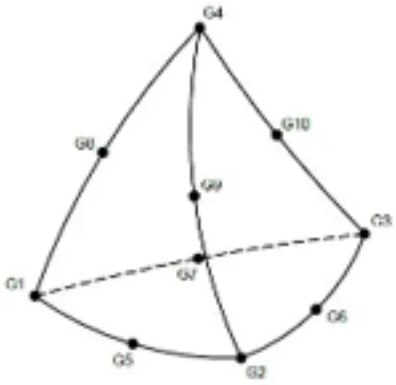


**Figure 7.3:** II order CTETRA.

the large ASCII-based **PCH** files, which can reach sizes of up to 64 GB. To manage this, the script was optimized to leverage parallel computing, enabling it to read and process the file in manageable blocks. To further reduce the weight of this file, it can be requested of Siemens Simcenter 3D to print out just the data related to the nodes selected in a group of interest, in this case, just the cubesat assembly without the platform elements. An alternative approach using Siemens Simcenter 3D's binary **HDF5** output was investigated; this format would permit significantly faster data access in MATLAB. However, its full implementation was deferred due to time constraints.
The VTK format (Figure 7.4) is used in the addon BlenDIC to import the object silhouette (just the shell) into Blender. This format requires the Nodes location, Connectivity and Displacement at iteration.
In the Figure 7.4, "n. vertex" is the number of nodes needed to define the polygon faces.

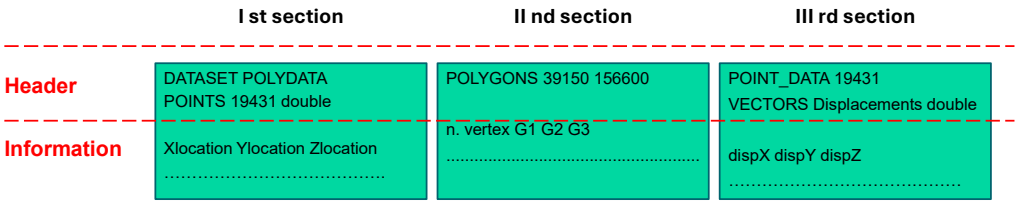


**Figure 7.4:** VTK file sections.

The format is a 0-based ID, which means that the information of the FEM model nodes' ID is not saved. The most time-consuming step is the displacement extraction, where an initial check defines the number of blocks for parallel computing. After the extraction, an additional step was introduced to export the temporal history of selected node indices, provided as vectors, into a **CSV** file, easy to read in the MATLAB environment. This enables a reference signal for comparison in subsequent steps, ensuring that the image analysis code reproduces the expected displacements at that same point of the FEM model. It should be emphasized that no simulation is performed in Blender. The displacement time history of the nodes belonging to the triangular elements of the outer shell (optionally amplified) is extracted from the simulation in Siemens Simcenter 3D.

## 7.3 Virtual Environment Setup in Blender

### 7.3.1 Model Import and Texture Application

The model import into Blender is a two-step process managed by the blenDIC plugin [21]. First, a static **VTK** file containing the initial mesh (outer shell, without the third section) is loaded. Subsequently, the sequence of time-dependent **VTK** files is imported as animation frames. Considerable challenge arose when applying the speckle pattern texture required for motion analysis. Since the plugin was primarily designed for single components, it applied the texture inconsistently across the assembly. Due to the complex, non-planar geometries, Blender's default texturing algorithm handled individual triangular faces independently. It attempted to fit the texture in the best possible way, resulting in a disorganized, non-uniform pattern. The issue was addressed by manually defining surface boundaries (Figure 7.5) and employing Blender's UV Editing tools, enabling the coherent mapping of a continuous texture across the surfaces of interest (Figure 7.6). A second distinct texture was also created to differentiate the plate from the main CubeSat structure, as the code relies on color contrast.

The speckled texture was eventually discarded in favor of a white texture with gray shades,

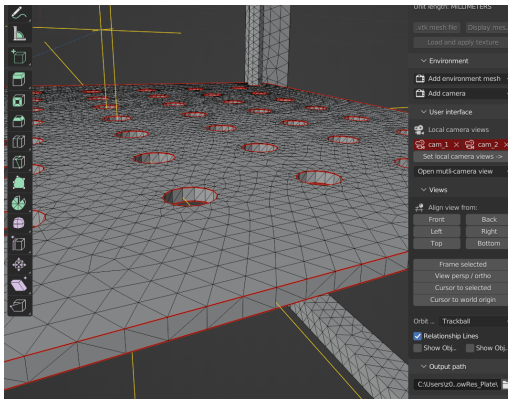

**Figure 7.5:** Edge Selection.

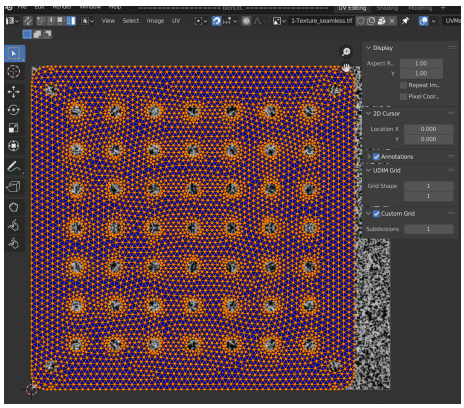

**Figure 7.6:** Face on Texture.

providing a more realistic representation of the white plate and adding a sense of roughness and detail to its surface Figure 7.7.

## 7.4 Virtual Camera Setup and Optimization

With the model correctly textured, the primary application of the virtual environment was to conduct a preliminary study of camera viewpoints for the physical test.

### 7.4.1 Camera View Setup

An initial setup involved positioning a virtual camera with its optical axis parallel to the surface of the plate, Figure 7.8.

**Figure 7.7:** Final Texture Setup.

The hypothesis was that this side-view perspective would be optimal for capturing the

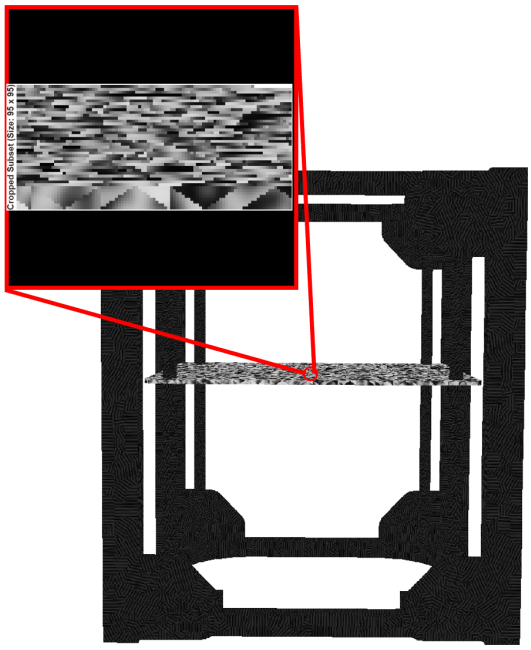

**Figure 7.8:** Analysis of Virtual Motion Video Results

plate's primary bending mode via the VMM code. However, analysis of the video rendered from this viewpoint revealed it was unsuitable. The VMM algorithm operates by averaging pixel displacement within a defined Region of Interest. From a side view, the crucial out-of-plane motion (Z-displacement) was averaged together with in-plane motion, effectively obscuring the critical displacement data. Based on this finding, subsequent configurations (Figure 7.9) focused on viewpoints that captured the plate's surface more directly, such as a 45-degree angled view. This optimized perspective ensures that the out-of-plane motion is distinctly observable as pixel displacement on the camera's sensor plane.

The use of VMM, as explained in Chapter 2, performed upon a virtual video generated through Blender, allows for the optimization of camera position, depth of field, and lens aperture prior to the physical experiment, significantly streamlining the setup phase. While

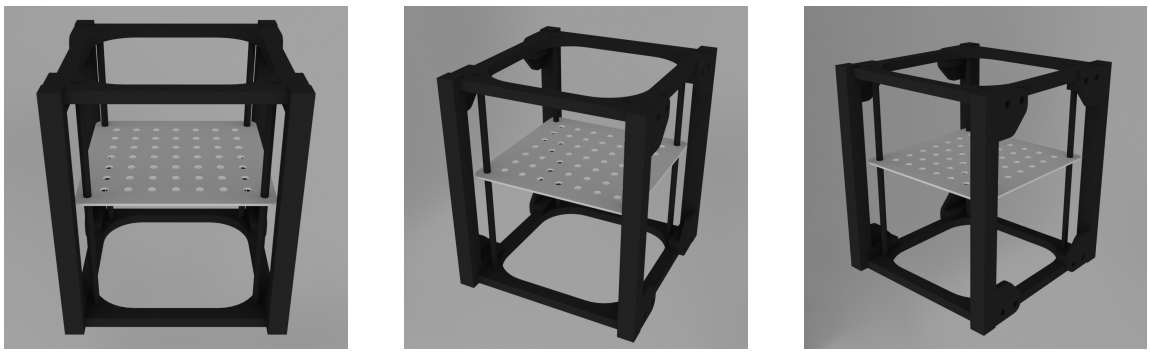

First Camera View. Second Camera View. Third Camera View.

**Figure 7.9:** Camera view of interest.

not fully explored, the environment also offers the capability to simulate lighting conditions and other critical experimental parameters.

## 7.5 Analysis of Virtual Motion Video Results

The analysis of videos from the optimized, angled viewpoints successfully identified the principal modes of oscillation of the plate.

### 7.5.1 First Camera View Analysis

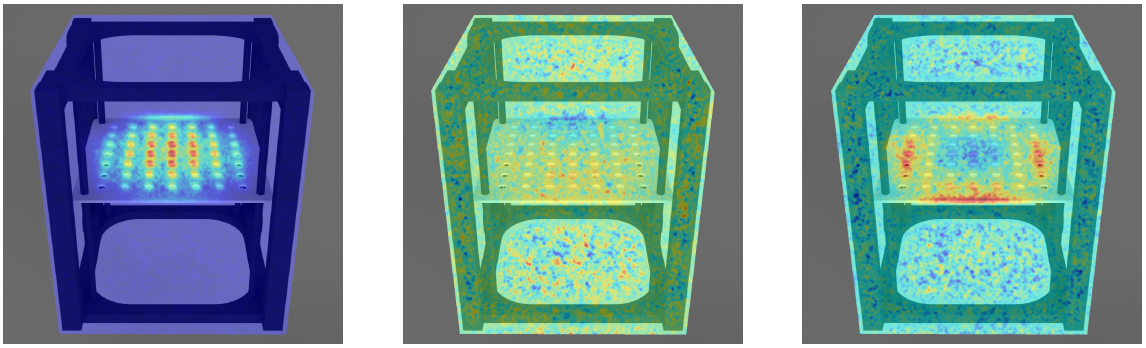

$f_1$ static ODS. $f_3$ static ODS. $f_4$ static ODS.

**Figure 7.10:** Static ODS of Camera 1.

The static maps of the ODSs shown in Figure 7.10 were captured by selecting peaks directly from the Power Spectrum (PS) sum graph as shown in Figure 2.3, helped by the PS contributions of the ROIs (Figure 7.11). It can be noted that most of these peaks are difficult to recognize. This aspect was further investigated in Section 7.5.4.

Within the PS an additional peak at 160 Hz was identified, following visualization of the magnified video, as the $f_2$ ODS of the structure. In this case the structure slightly shift in the right-left direction resambling the ODS from Figure 6.3.

The frequencies obtained from the magnification process are reported in Table 7.1.

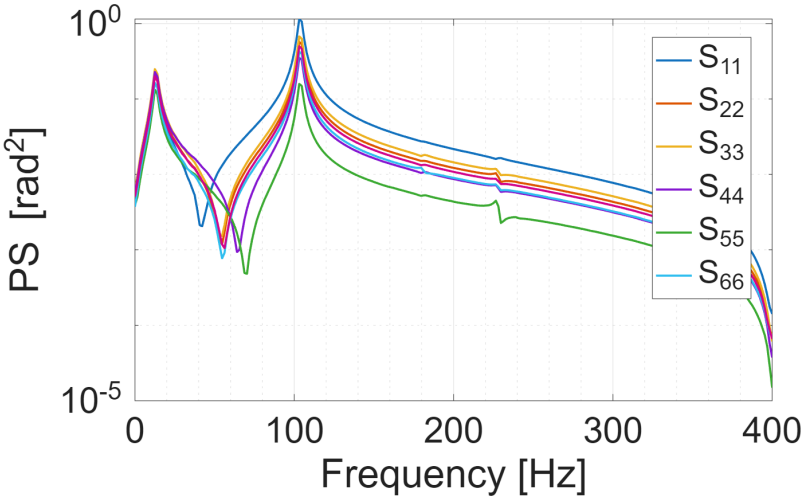


**Figure 7.11:** ROIs PS contribution.

**Table 7.1:** Frequencies Selected.

| $f_1$ | $f_2$ | $f_3$ | $f_4$ |
|---|---|---|---|
| 103.78 Hz | 161.23 Hz | 180.97 Hz | 227.90 Hz |

### 7.5.2 Second Camera View Analysis

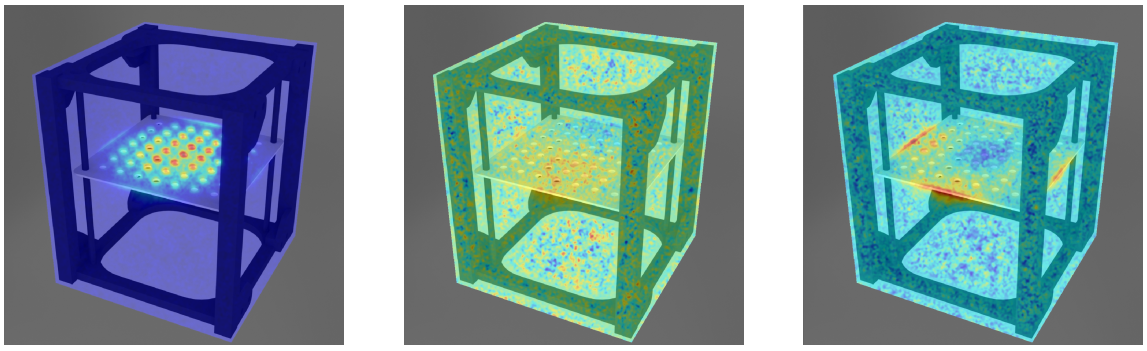

$f_1$ static ODS. $f_3$ static ODS. $f_4$ static ODS.

**Figure 7.12:** Static ODS of Camera 2.

As can be observed, the captured ODS (shown in Figure 7.12) for the second camera are the same, but this camera appears to reveal the intensities better, thanks to the better view of the plate plane.
The $f_2$ frequency of interest, shown in Table 7.1, is captured as well.

### 7.5.3 Third Camera View Analysis

Similarly, the ODS captured by the third camera are the same (Figure 7.13). However, during the visualization of the results, it was observed that the presence of the column

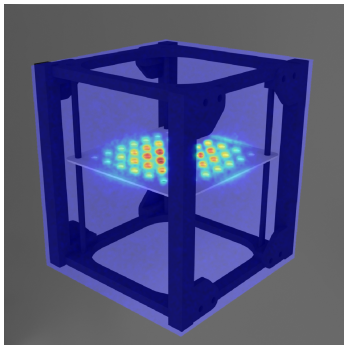

$f_1$ static ODS.

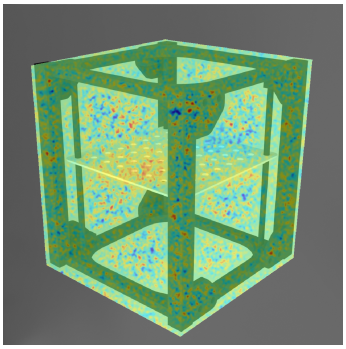

$f_3$ static ODS.

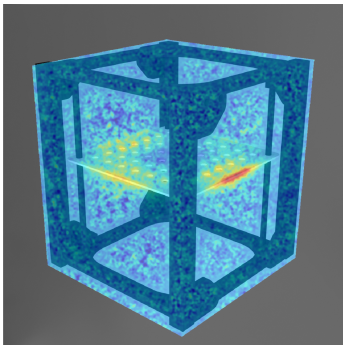

$f_4$ static ODS.

**Figure 7.13:** Static ODS of Camera 3.

at the central point could disturb the visualization of the plate plane. Consequently, this camera view was abandoned in favor of the other two camera perspectives.

### 7.5.4 Investigation of Low-Level Mode Visibility

Only a limited number of distinct peaks were observed in the Blender-generated videos when compared with the mode shapes expected from the modal analysis results presented in Section 6.2.3. The mode corresponding to the plate's fundamental vibration was clearly identifiable, whereas the higher-order modes were not distinctly visible. As a first step, it was necessary to investigate the possible causes of this discrepancy. Since the video had been rendered in Blender and subsequently processed using the VMM code, the issue had to originate either from the VMM processing sequence or the transient FE simulation itself. Given that no anomalies had been encountered during the transient analysis, the initial assumption was that the problem might lie within the VMM computation. To verify this hypothesis, the displacement time histories were extracted from two areas of interest on the plate (Figure 7.14) obtained from the transient FE analysis. Subsequently, corresponding ROIs were defined on the camera detector. These ROIs were square areas centered on the same physical locations of the plate as viewed in the rendered video. Within each ROI, the displacement of the pixels along the u and v directions of the camera detector was extracted. The extracted signals were then processed using the omalscf function, a routine developed by MIT that computes the PS of the motion signal, allowing for the identification of dominant vibration frequencies. The results obtained from the displacement time histories of the FEM model are shown in Figure 7.15 , while those obtained from the camera detector displacements are reported in Figure 7.16.

The units of measurement differ between the two datasets, and the displacements obtained from the finite element model are significantly smaller than the pixel-based quantities. This discrepancy arises because the FE model operates in meters, which results in extremely small numerical values for local displacements. Nonetheless, it is still possible to compare the magnitude of the signals for each area of interest. As shown, the overall trends are quite similar between the FEM displacement signals and those extracted from the corresponding

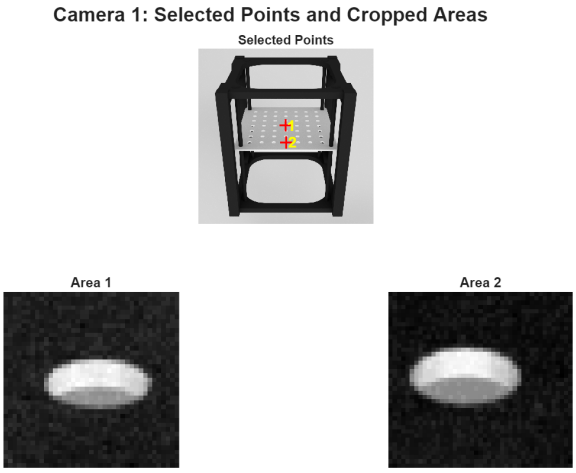


**Figure 7.14:** Area selected.

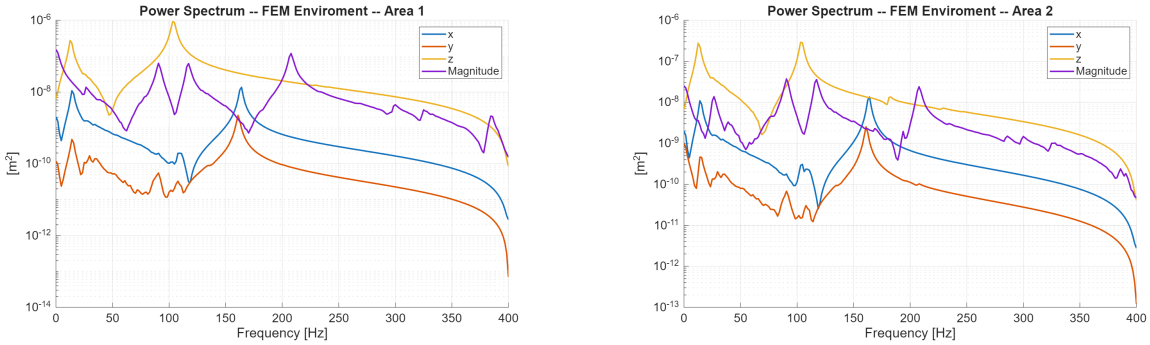


**Figure 7.15:** Siemens Simcenter 3D Enviroment.

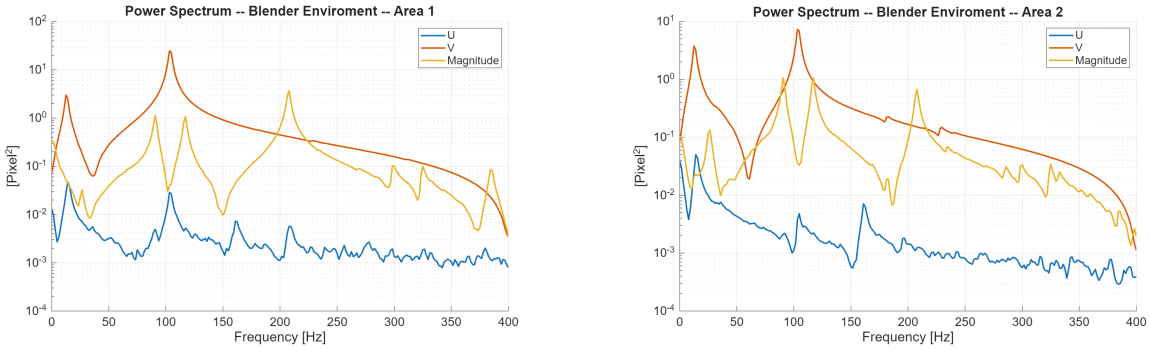


**Figure 7.16:** Blender environment.

regions in the video. Therefore, the attenuation of the secondary peaks in the power spectrum does not appear to be related to the VMM processing itself, but rather to another factor within the analysis chain.

Another potential weak point in the analysis chain was the excitation signal applied by the shaker. It is possible that during the implementation or handling of this input signal, its characteristics were unintentionally altered. This analysis ultimately revealed that the issue did not originate from the VMM code. In fact, by observing the magnitude profiles for the same regions of interest, the signals exhibit consistent trends despite their different units and amplitudes. Nevertheless, it was still possible to generate amplified videos showing the relative ODS by selecting frequency peaks identified through the PS summation graph

in Figure 7.11. These results demonstrate the robustness and applicability of the method, even when the simulated excitation conditions differ from ideal experimental setups. This virtual testing phase proved invaluable for defining the physical test setup and developing proficiency in selecting appropriate ROIs for the motion analysis algorithm. The preliminary results from this virtual analysis will be a direct reference for the data acquired during the physical MIMO control test.

# Chapter 8

# Environmental Vibration Test

## 8.1 Test Workbench Configuration and CubeSat Mounting

The CubeSat was mounted on the platform, ensuring its positioning was consistent with the Siemens Simcenter 3D model developed in Chapter 6. To replicate a fixed condition similar to that established in Chapter 6.2.2, a metal plate was utilized to clamp the lower part of the structure. Care was taken to ensure this plate did not obstruct the area designated for camera inspection. It was secured using six screws, with meticulous attention paid to the applied tightening torque. The plate was thus fixed to prevent structural movement without introducing additional constraints that could induce stresses that could lead to structural failure or alteration of the results. This was experimentally confirmed during the test (due to observed platform control issues) and by hearing, as the improperly secured plate produced sharp noises at high frequencies.

### 8.1.1 Accelerometer Instrumentation for Platform Control

The platform was instrumented with two three-dimensional accelerometers placed congruently with the Siemens Simcenter 3D model reference system axes (Figure 8.1), on the plate where the satellite is mounted, for test control. A smaller three-dimensional accelerometer (1 gram mass) was applied near the center of the plate (Figure 8.2).

This accelerometer measured the plate displacements via cameras to provide a qualitative assessment of the frequencies expected from subsequent structural analysis. It is acknowledged that this component would increase the mass on the plate and slightly alter the modes.

### 8.1.2 Multi-Shaker Excitation System

The test system consists of four shakers connected to four amplifiers. These are interfaced with a Simcenter SCADAS Mobile (SCM05) system, which serves as both the signal generator and data acquisition system. The Simcenter SCADAS generates four partially correlated drive signals to excite the four shakers. Four control channels (accelerometers) evaluate the system responses and ensure the vibration is on target in all directions via

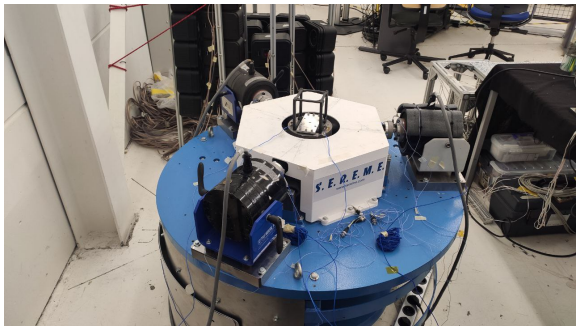


**Figure 8.1:** Platform S.E.R.E.M.E.

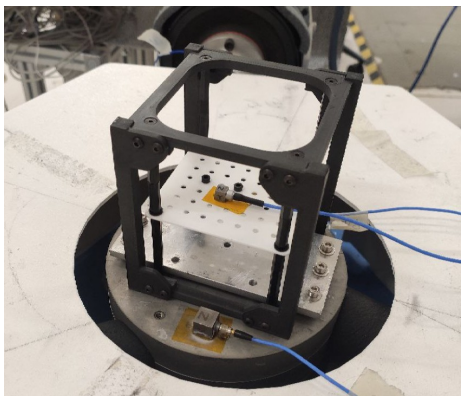

**Figure 8.2:** CubeSat instrumented.

MIMO control.
In addition, a button providing the signal for measuring the camera trigger was connected to the Simcenter SCADAS and the camera Hardware.

## 8.2 TestLab Configuration for MIMO Random Control

### 8.2.1 SCADAS Channel Setup and Sensitivity Definition

The instrumentation connected to the Simcenter SCADAS in the channel setup window was defined with its respective characteristics and sensitivities. For each, a name was assigned to ensure consistency with the profile to be followed, which was retrieved from the VEGA C manual [19]. The configuration of the selected channels connected to the Simcenter SCADAS system is detailed in Table 8.1.

The accelerometers located at Points P2 and P4 are designated as the primary control

**Table 8.1:** Selected Simcenter SCADAS Channel Configuration

| Physical Channel | On/Off | Channel Group | Point | Direction | Input Mode | Coupling | Measured Quantity | Actual Sensitivity |
|---|---|---|---|---|---|---|---|---|
| Input1 | ✓ | Control | P2 | +X | ICP | Single Ended | Acceleration | 101.3 mV/g |
| Input2 | ✓ | Control | P2 | +Y | ICP | Single Ended | Acceleration | 99.1 mV/g |
| Input3 | ✓ | Control | P2 | +Z | ICP | Single Ended | Acceleration | 101.4 mV/g |
| Input4 | ✓ | Control | P4 | +X | ICP | Single Ended | Acceleration | 99.34 mV/g |
| Input5 | ✓ | Measure | P4 | +Y | ICP | Single Ended | Acceleration | 97.94 mV/g |
| Input6 | ✓ | Measure | P4 | +Z | ICP | Single Ended | Acceleration | 96.48 mV/g |
| Input7 | ✓ | Measure | T1 | +X | ICP | Single Ended | Acceleration | 5.13 mV/g |
| Input8 | ✓ | Measure | T1 | +Y | ICP | Single Ended | Acceleration | 5.19 mV/g |
| Input9 | ✓ | Measure | T1 | +Z | ICP | Single Ended | Acceleration | 5.22 mV/g |
| *...Channels 10-24 are not connected to any instrumentation...* | | | | | | | | |
| Input25 | ✓ | Measure | TRIGGER | S | Voltage AC | Single Ended | Acceleration | 100 mV/g |

points for controlling the platform during the test. T1 is the accelerometer positioned on the plate to monitor is behaviour trought the test. These channels will be actively checked during the test to ensure the platform's control. At least four directions of control are required to manage the four degrees of freedom of the platform. The nomenclature used for these control points within the system configuration must precisely match the definitions imported from the Cross-Power Matrix.

### 8.2.2 MIMO Random Test Setup: Profile and Safety Parameters

MIMO Random Setup is defined, where the reference profile table is imported externally. This table defines the platform control and is constructed from the VEGA C launch profile. The control loop is defined in the "MIMO Random Mode" panel. The frequency resolution is set to 0.78125 Hz, with a minimum frequency of 25.00 Hz and a maximum of 1000.00 Hz. Safety parameters include an RMS Abort threshold of 12.00 dB and a Build-up/down time of 2.00 seconds. For safety reasons, a build-up profile was also defined, setting a step at a slightly lower power (-3.00 dB Startup level) for 30 seconds (Equalization time: 0:00:30.00), followed by a final one at maximum power for one minute (Full level time: 0:01:00.00). This full-level duration is consistent with the maximum measurable time length from the camera settings, discussed in the next section. The cross-correlation matrix sets amplitude levels for different control channels as depicted in the "Cross-Power Matrix" Figure 8.3. For instance, P2:+X has a control amplitude of 0.767 g, with cross-correlations of 0.05 with P2:+Y and P2:+Z, and a high cross-correlation of 0.98 with P4:+X. This setting ensures the platform channels record coherent displacement, preventing platform rotation.

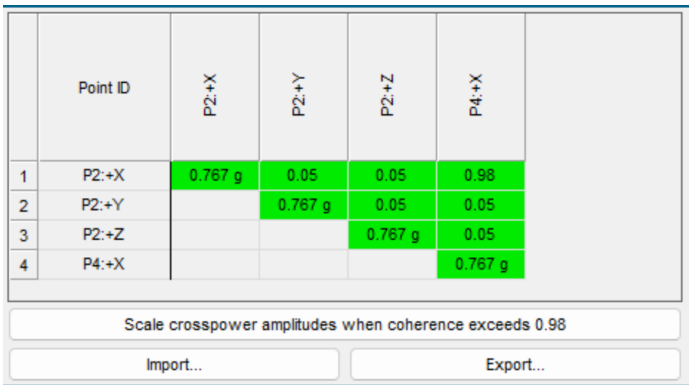


**Figure 8.3:** Control Matrix.

### 8.2.3 System Identification and Verification Procedures

Subsequently, the System Identification phase is initialised, where the system matrix is constructed, and it is verified that the MIMO platform works as expected. Shaker 4's output (the one responsible for the Z-direction excitation) must be higher because it is a different shaker with higher power to support the platform's weight. During system identification, we can verify that the system matrix is correctly calculated and that the structure is scanned with a low-intensity white noise signal. A pre-test analysis is performed in the System Verification step. By accessing the coherence of the four control channels, we ensure the control test will be performed safely and successfully (Figure 8.4). Once the predicted responses align with expectations, we can proceed with the actual control test.

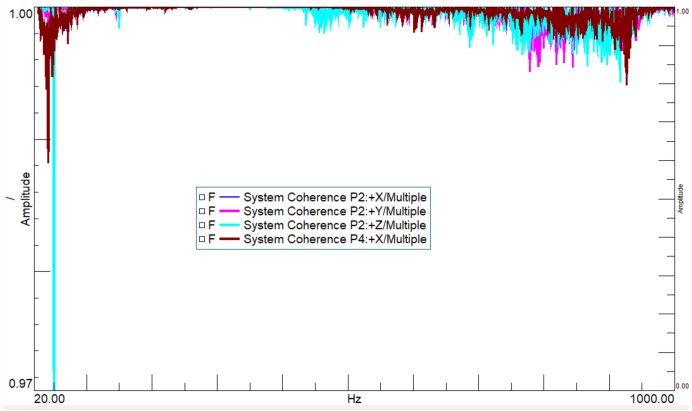


**Figure 8.4:** Coherence Measurement of the control signals defined during System Verification.

### 8.2.4 Execution of the Random Control Test

The actual MIMO Random Control Test is initiated if no significant issues are detected. Once this procedure starts, the four control channels can be monitored to ensure the signal adheres to safety margins, which is more clearly visible in the right-hand panel, where these quantities are displayed numerically. Simultaneously, we can monitor, for example, the acceleration in the Z direction to begin observing where the first peaks are located. If everything is performed correctly, these should coincide with the plate's natural modes. At the end of the operation, the figure 8.5 of the control channel was obtained, proving that the test was successful.

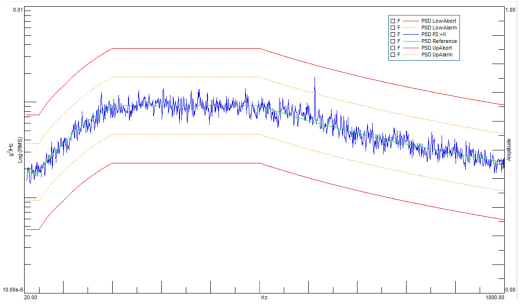

Point P2 +X.

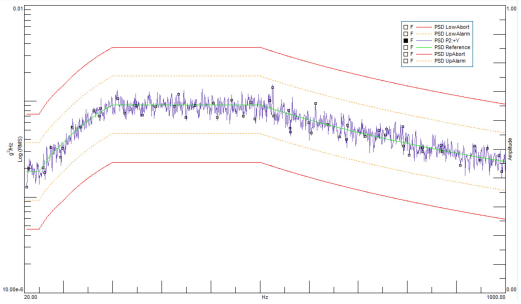

Point P2 +Y.

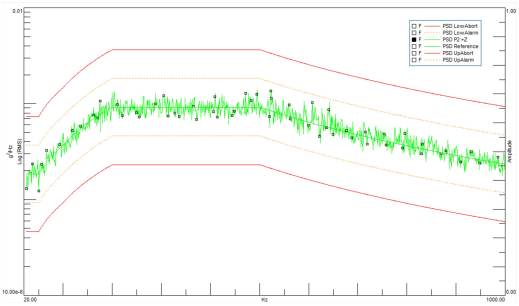

Point P2 +Z.

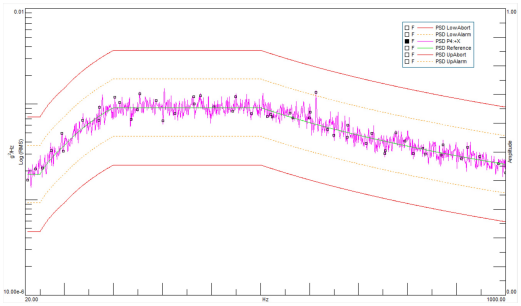

Point P4 +X.

**Figure 8.5:** Control Channels.

## 8.3 Vibration Test Results and Modal Correlation

By selecting the "Navigator" button in Simcenter Testlab, the test results can be accessed, enabling the creation of a plot displaying the PSDs of the three measurement channels of the T1 accelerometer (Figure 8.6). Analyzing these three profiles, potential natural frequencies were selected based on their distinct peaks. Subsequently, by examining the magnitude of the mode shapes derived from the modal analysis presented in Chapter 6.2.3, possible correlations were established and are documented in the table 8.2.

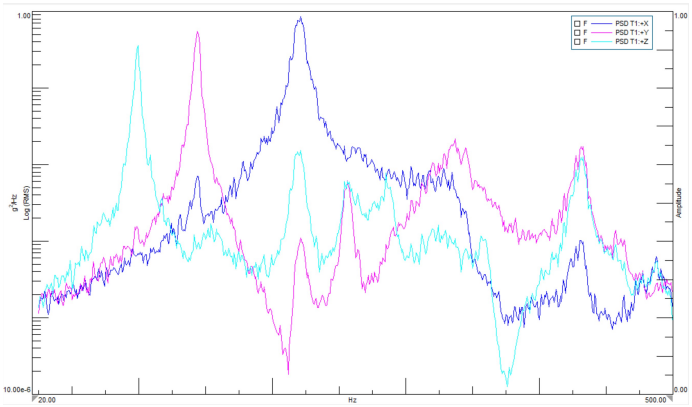


**Figure 8.6:** PSD of measurement X-Y-Z overlayed

## 8.4 High-Speed Camera Setup and Acquisition

For video acquisition, the Ix Camera Series 510 was used, with a resolution of 1080×1080, providing a high level of detail for the scene.

### 8.4.1 Camera Parameters and I-Speed Software Configuration

The camera was operated using the I-speed control software, which allowed for the definition of the desired frame rate and to set the frame size and the shutter speed through the windows in Figure 8.7. Knowing the camera positions beforehand, as established in Chapter

| Mode | Frequency | Description |
|---|---|---|
| 1st | **99.46 Hz** | First plate mode (one bump) |
| 2nd | **144.00 Hz** | Side swing Y-direction |
| 3rd | **223.46 Hz** | Side swing X-direction |
| 4th | **258.38 Hz** | Plate mode (weight direction, two bumps) |
| 5th | **287.27 Hz** | Plate mode (previous shape rotated 90°) |
| 6th | **337.64 Hz** | Plate rotation |
| 7th | **428.13 Hz** | Plate mode |

**Table 8.2:** Frequencies and descriptions of vibration modes

7, resulted in a faster camera setup.

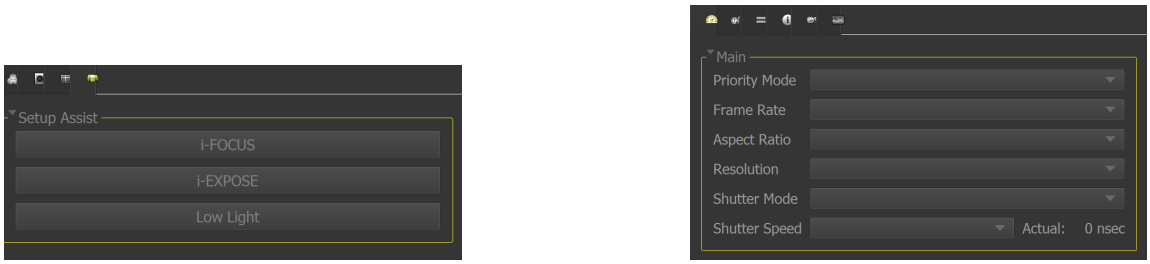


**Figure 8.7:** I-speed software windows.

### 8.4.2 Lighting and Camera Positioning for Optimal Visibility

However, the positioning of the lights was more counterintuitive. The exposure was controlled by specific windows in the I-speed software, Figure 8.7. The camera's trigger was connected to the Simcenter SCADAS via a channel to control the active acquisition of the camera, although this signal was not ultimately used.

### 8.4.3 Video Acquisition Procedure and Data Management

The cameras were activated during the one-minute full power phase, recording approximately 53 seconds of testing. However, due to the significant volume of data, it was deemed appropriate to save 4 seconds for each set, encompassing both the 800 Hz and 1600 Hz cases. The datasets acquired with a sampling rate of 1600 Hz were discarded due to the computational limitations of the MATLAB code.

## 8.5 Experimental Video Analysis Results

The real experimental videos, where the excitation was more uniformly distributed across the structure, after going through the VMM process, exhibited frequency peaks consistent with the expected modal shapes. Those peaks resulted in slightly lower resonance frequencies, as anticipated. This shift was attributed primarily to the added accelerometer mass, which influenced the modal frequencies without introducing additional modes within the analyzed frequency range. The static plotting, used in Section 7.5, was unsuccessful for all the modes in this case. Considering the nature of oscillatory motion, which is defined by its displacement relative to a static equilibrium, it was deemed most illustrative to present three specific frames. These frames sequentially capture the maximum positive displacement (peak), the zero-displacement (static) state, and the maximum negative displacement (opposite peak) of the oscillation. The results were consistent across the measurement and enabled a qualitative yet reliable identification of modal behavior, which would have been difficult to achieve with only a single accelerometer.

### 8.5.1 First Camera View: ODS Key Frames

**Table 8.3:** Frequencies Selected.

| $f_1$ | $f_2$ | $f_3$ | $f_4$ | $f_5$ | $f_6$ | $f_7$ |
|---|---|---|---|---|---|---|
| 98.09 Hz | 143.27 Hz | 220.02 Hz | 257.47 Hz | 285.72 Hz | 340.26 Hz | 358.67 Hz |

A detailed analysis of its natural frequencies and corresponding mode shapes has been conducted to provide a comprehensive understanding of the structure's dynamic characteristics. Complemented by illustrative key frames, the following descriptions elucidate the specific vibrational patterns observed at each identified natural frequency.

The first natural frequency, $\mathbf{f_1 = 98\ Hz}$, as depicted in Figure 8.8, is characterized by a fundamental bending behavior. This mode primarily involves a single, prominent oscillation of the central region of the plate.

Moving to $\mathbf{f_2 = 143\ Hz}$, illustrated in Figure 8.9, the mode manifests as a global lateral oscillation of the entire structure. This motion is predominantly observed along the Y-direction, indicating a sway or shear-like deformation of the CubeSat platform.

For the third natural frequency, $\mathbf{f_3 = 220\ Hz}$, referenced in Figure 8.10, the structure exhibits a more complex bending pattern. This mode is characterized by two distinct curvatures, or antinodes, developing along the direction aligned with the masses, suggesting a higher-order bending mode specific to that orientation.

At $\mathbf{f_4 = 257\ Hz}$, as shown in Figure 8.11, a significant torsional response is observed. This mode is defined by a simultaneous rotation of the entire structure around its Z-axis, indicating a twisting deformation superimposed on other potential motions.

The fifth natural frequency, $\mathbf{f_5 = 285\ Hz}$, presented in Figure 8.12, reveals another bending pattern along the Y-direction. However, in this mode, the two curvatures are phase-opposed to the direction of the masses, signifying a more intricate and distributed bending pattern compared to the mode observed at $f_3$.

Figure 8.13 illustrates the mode shape corresponding to $\mathbf{f_6 = 340\ Hz}$. This mode is notably characterized by a central point experiencing maximal downward displacement. Concurrently, the four peripheral edges of the square plate move upwards, resulting in a dish-like or dome-like deformation across the structure.

Finally, at $\mathbf{f_7 = 358\ Hz}$, as detailed in Figure 8.14, the structure exhibits a distinctive "saddle-like" deformation. Here, the edges of the plate parallel to the Y-axis move upwards, while those parallel to the X-axis simultaneously undergo a downward displacement. This creates a characteristic anti-clastic curvature across the platform.

These visual representations, derived from the VMM analysis, offer invaluable insights into the complex dynamic behavior of the CubeSat platform at its various natural frequencies, complementing the numerical data with clear qualitative identification of the mode shapes.

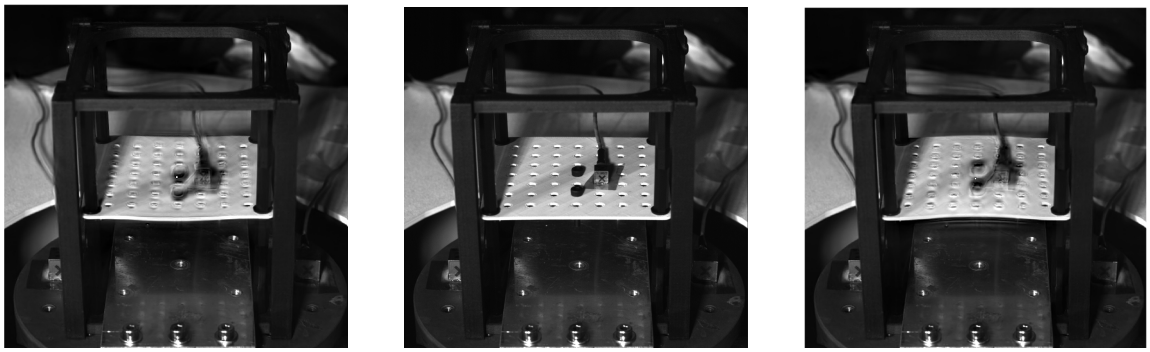

**Figure 8.8:** Camera 1 - Key Frames of Motion for the first natural frequency ($f_1 = 98$ Hz).

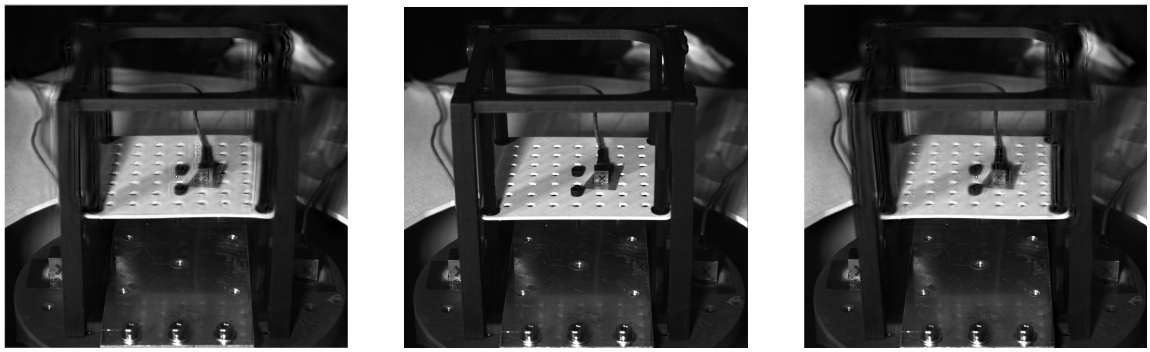

**Figure 8.9:** Camera 1 - Key Frames of Motion for the second natural frequency ($f_2 = 143$ Hz).

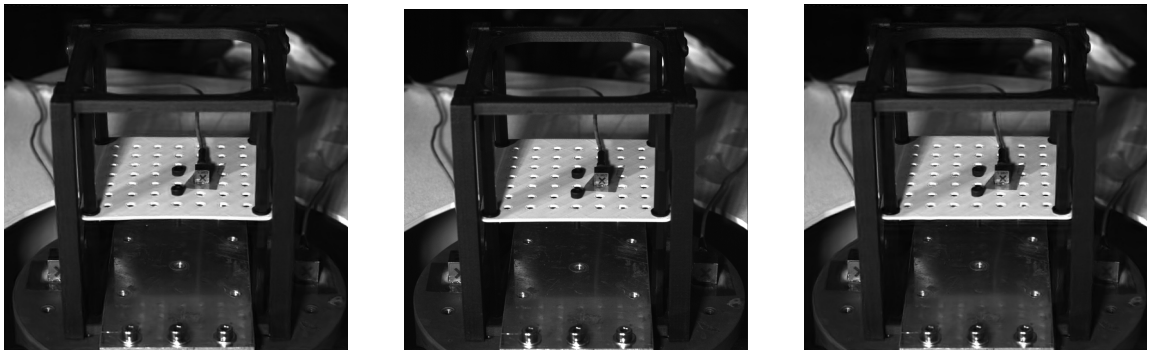

**Figure 8.10:** Camera 1 - Key Frames of Motion for the third natural frequency ($f_3 = 220$ Hz).

### 8.5.2 Second Camera View: ODS Key Frames

The results obtained by this camera view are similar to those obtained from camera one, listed in the Table 8.3, and are shown in the Figures from 8.15 to 8.21. In this case, the $f_3$ was easier to identify (Figure 8.17), because of the better view of the plate and the use of an angle that permitted evaluating the X direction displacement more easily than the previous configuration.

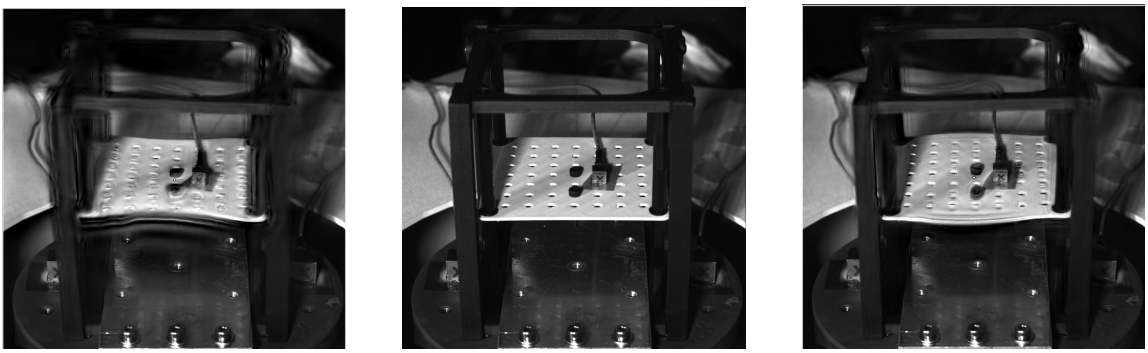

**Figure 8.11:** Camera 1 - Key Frames of Motion for the fourth natural frequency ($f_4 = 257$ Hz).

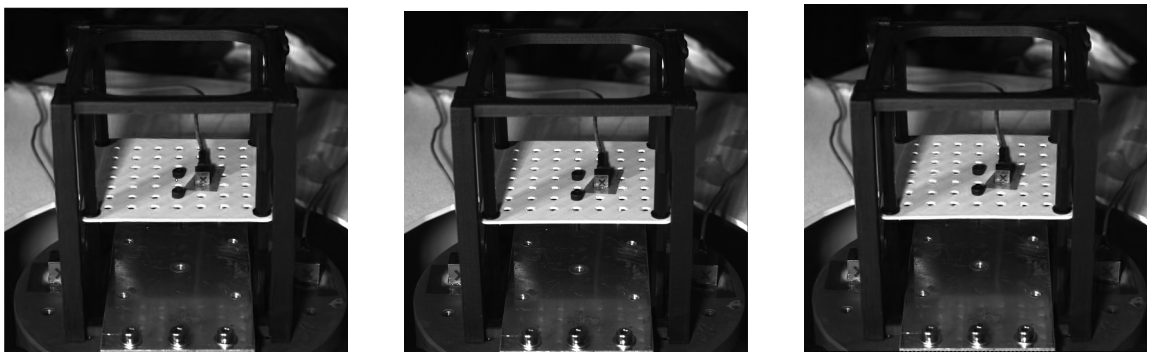

**Figure 8.12:** Camera 1 - Key Frames of Motion for the fifth natural frequency ($f_5 = 285$ Hz).

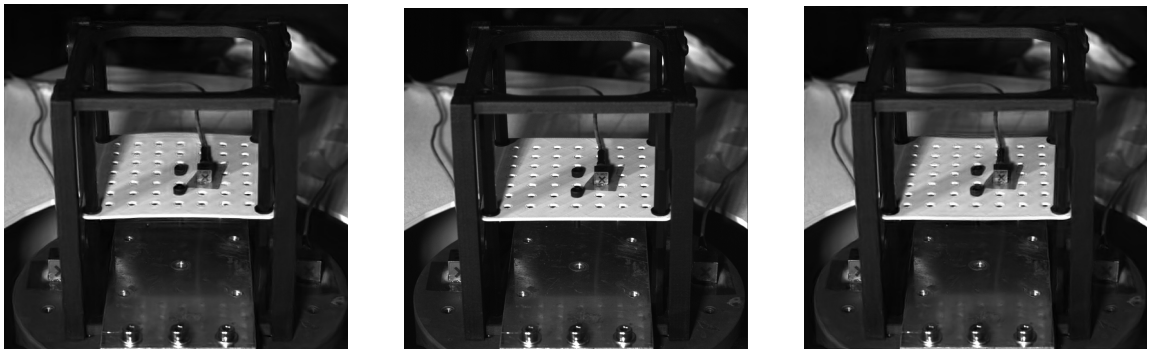

**Figure 8.13:** Camera 1 - Key Frames of Motion for the sixth natural frequency ($f_6 = 340$ Hz).

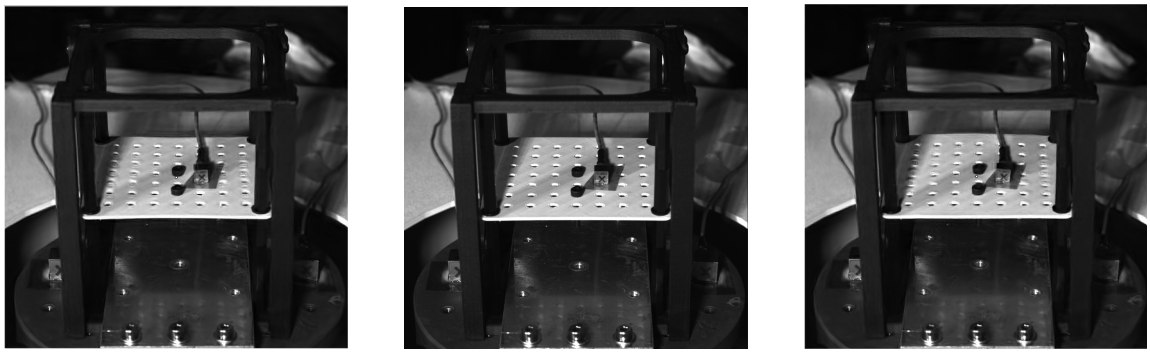

**Figure 8.14:** Camera 1 - Key Frames of Motion for the seventh natural frequency ($f_7 = 358$ Hz).

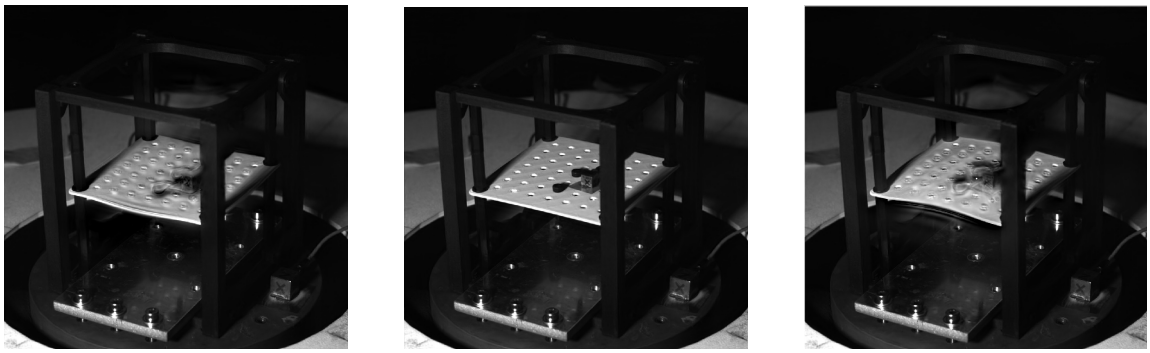

**Figure 8.15:** Camera 2 - Key Frames of Motion for the first natural frequency.

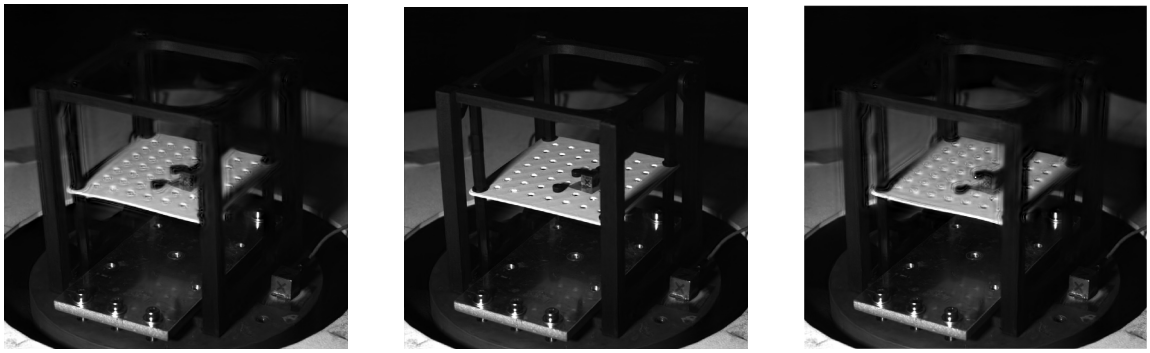

**Figure 8.16:** Camera 2 - Key Frames of Motion for the second natural frequency.

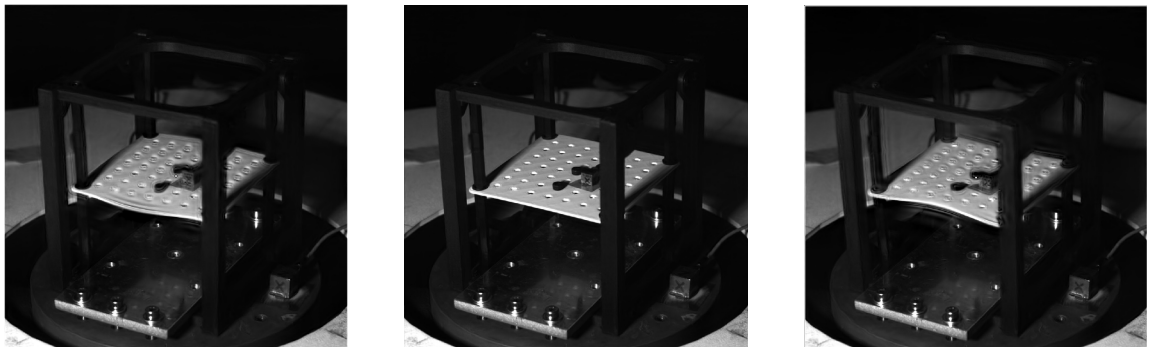

**Figure 8.17:** Camera 2 - Key Frames of Motion for the third natural frequency.

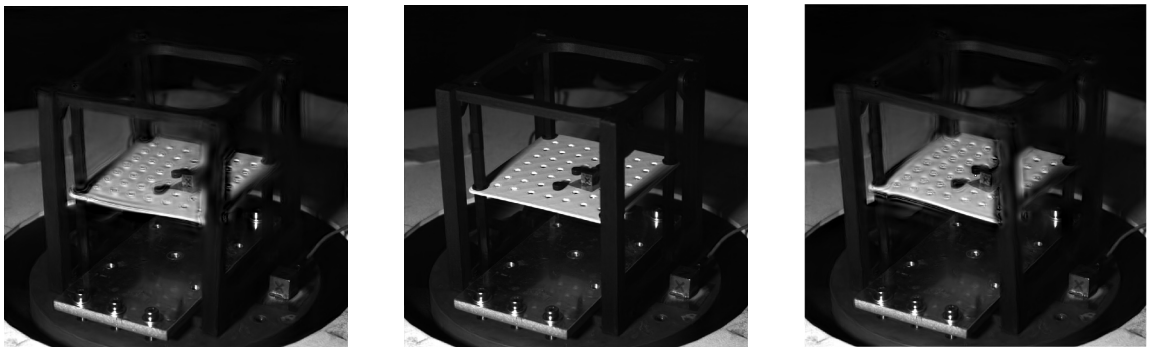

**Figure 8.18:** Camera 2 - Key Frames of Motion for the fourth natural frequency.

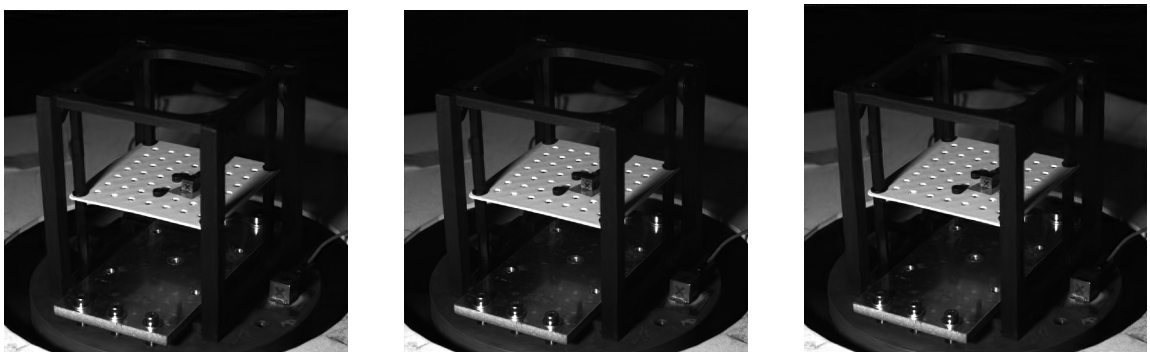

**Figure 8.19:** Camera 2 - Key Frames of Motion for the fifth natural frequency.

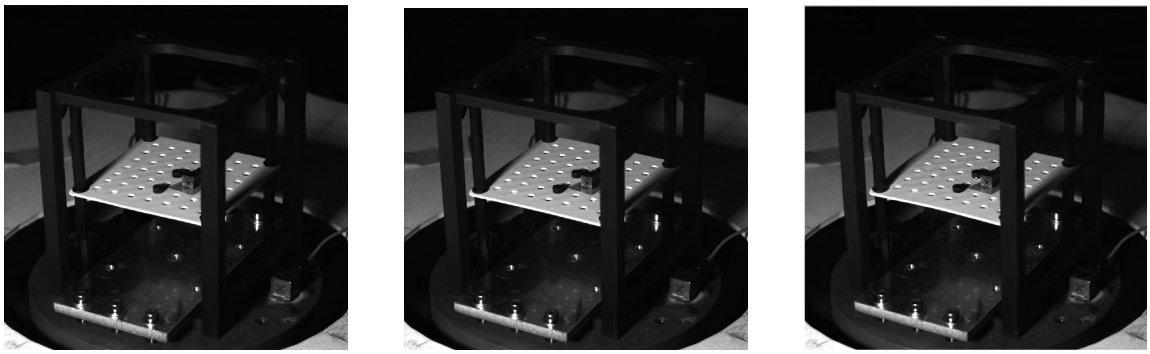

**Figure 8.20:** Camera 2 - Key Frames of Motion for the sixth natural frequency.

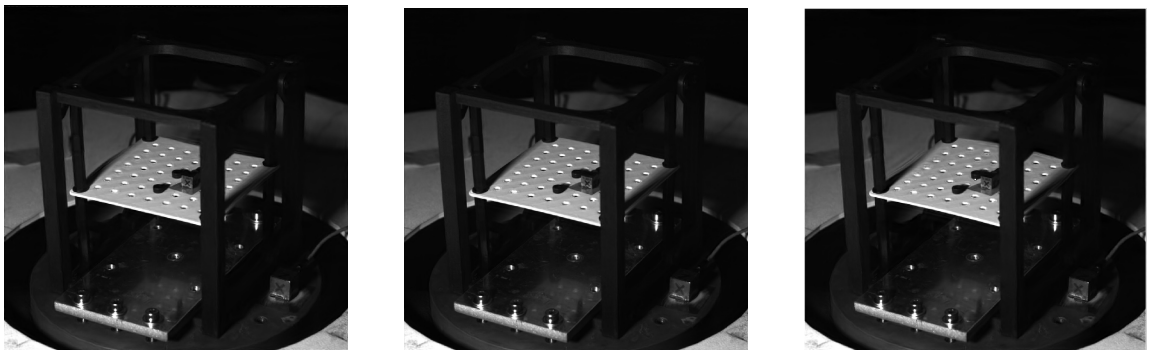

**Figure 8.21:** Camera 2 - Key Frames of Motion for the seventh natural frequency.

# Chapter 9

# Conclusions

This thesis successfully validates VMM as a robust pre-test and diagnostic tool for dynamic characterisation of aerospace hardware in vibration control tests. A key innovation was integrating VMM with a virtual pre-testing phase in Blender, which optimised camera positioning and predicted the dynamic response of a 3D-printed CubeSat dummy. This virtual-to-real workflow can potentially enhanced subsequent physical tests' efficiency, predictability, and cost-effectiveness. The research found strong agreement between VMM observations from the physical setup and expected dynamic behaviours. VMM applied to video footage clearly visualised the main operational deflection shapes and verified boundary conditions during Random Control Test pre-testing. While the Finite Element Method analysis indicated areas for improvement, the VMM results from the experimental setup showed satisfactory agreement with expected structural responses, affirming its reliability for preliminary design validation. The results demonstrate VMM's capacity to deliver rapid, non-invasive, and qualitatively rich information on structural dynamics. Its ability to amplify imperceptible motions from standard video footage without dedicated markers drastically reduces instrumental complexity and experimental preparation time compared to traditional methods. In conclusion, VMM is an invaluable complementary tool for preliminary design validation and pre-test analysis, enhancing efficiency and insight in dynamic characterisation workflows for aerospace and other critical engineering applications.

## 9.1 Future Work

Future research should focus on a more comprehensive assessment of various environmental and experimental parameters, including detailed analysis of optimal lighting conditions, precise camera positioning, and the influence of ambient noise on data quality. It is also critical to improve the simulation setup within Blender to achieve more uniform and realistic excitations, thereby enhancing the correlation with physical tests. Furthermore, efforts should focus on enhancing modal visualisation accuracy and processing efficiency. Although the average processing time of approximately 4000 seconds per mode was deemed acceptable for this analysis, continuous improvements in computational algorithms and hardware integration could significantly reduce these demands, thereby increasing VMM's

attractiveness for routine application. The ability to visualise and interpret complex mode shapes directly from video data holds immense promise for advancing structural health monitoring, design optimisation, and fault detection in critical engineering applications.

# Appendix A

# Appendix A

## A.1 Additional Figure from Chapter 5.

In this section of the Appendix are shown the remaining Figure of coherence measurament and modal fit operation for the remaining configurations.

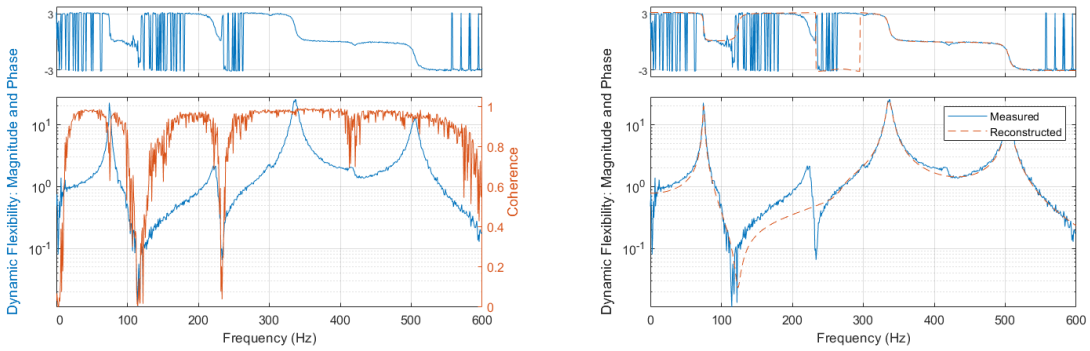


**Figure A.1:** Test Plate A mass 8.7 gr.

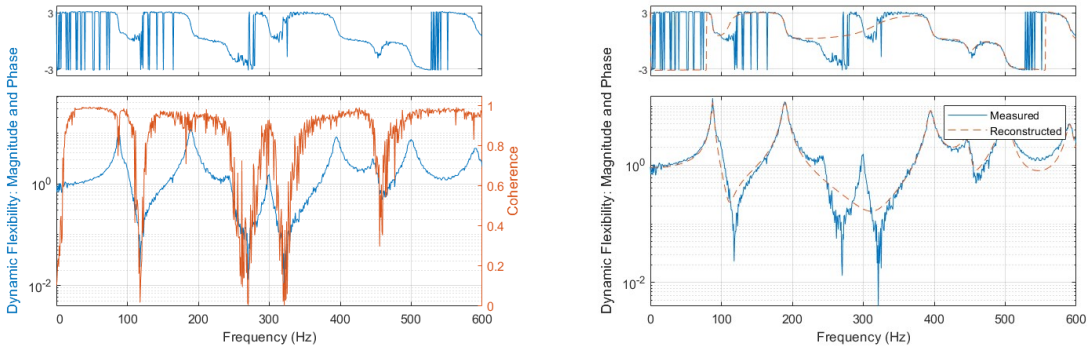


**Figure A.2:** Test Plate B mass 6.5 gr.

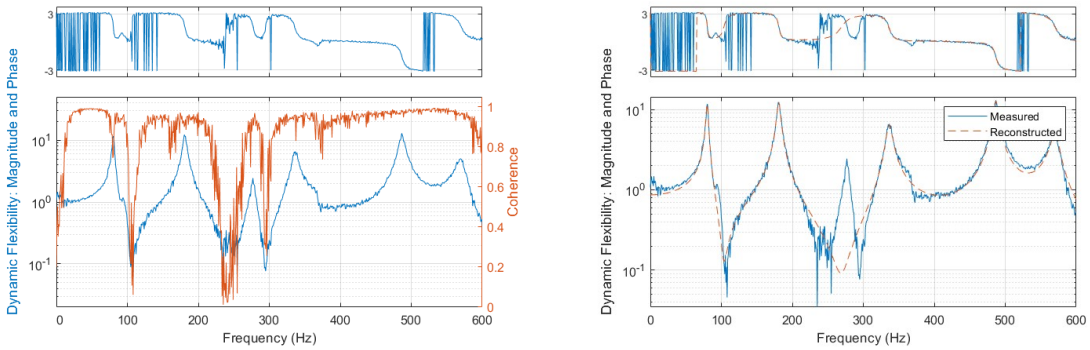


**Figure A.3:** Test Plate B mass 8.7 gr.

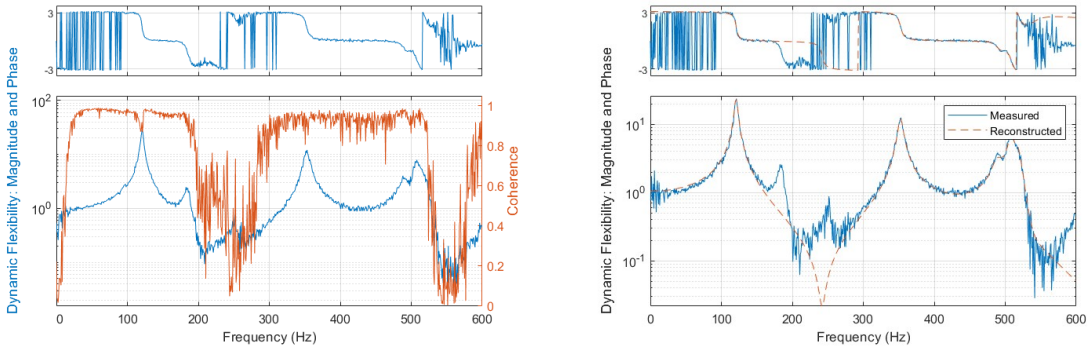


**Figure A.4:** Test Plate C mass 6.5 gr.

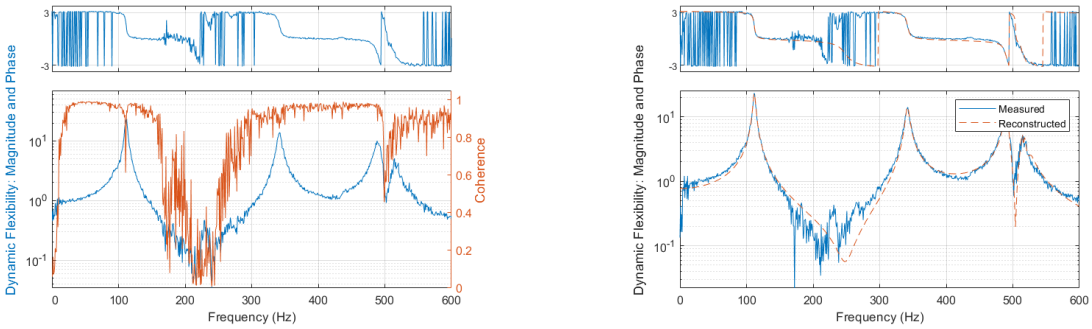


**Figure A.5:** Test Plate C mass 8.7 gr.

## A.2 Additional Figure from Chapter 6.

In this section of the Appendix are listed the remaing frequencies of interest obtained from the modal analysis of the assembly.

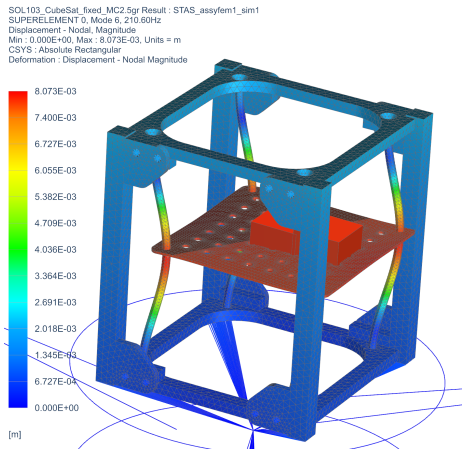


**Figure A.6:** $f_3$ of the CubeSat dummy model.

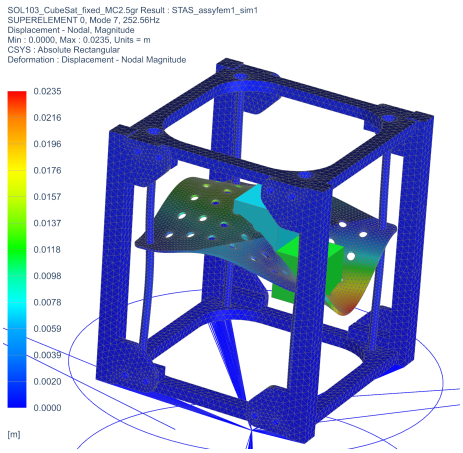


**Figure A.7:** $f_4$ of the CubeSat dummy model.

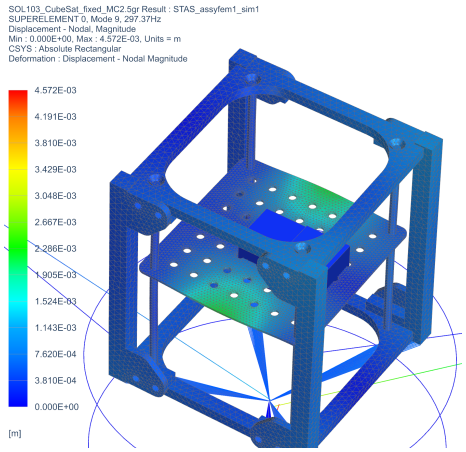


**Figure A.8:** $f_5$ of the CubeSat dummy model.

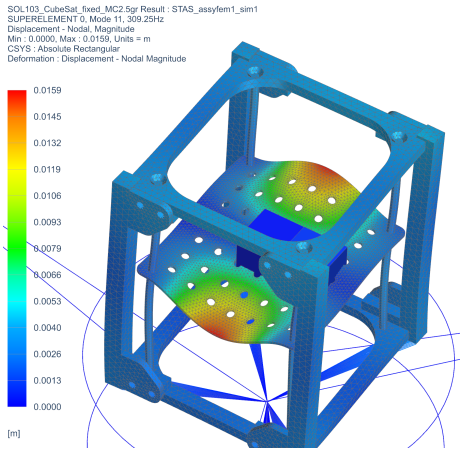


**Figure A.9:** $f_6$ of the CubeSat dummy model.

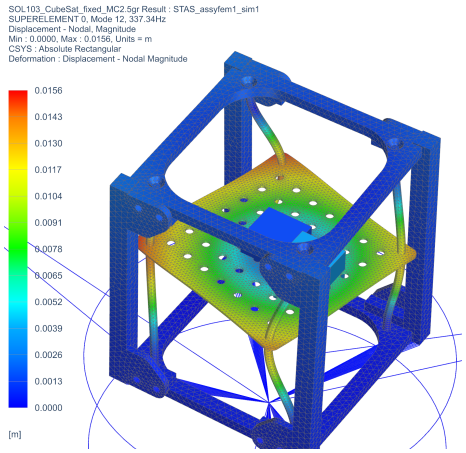


**Figure A.10:** $f_7$ of the CubeSat dummy model.

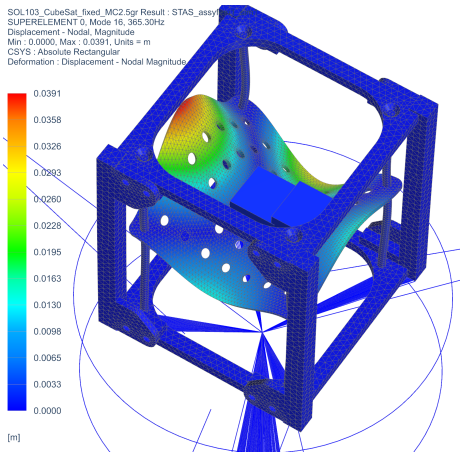


**Figure A.11:** $f_8$ of the CubeSat dummy model.

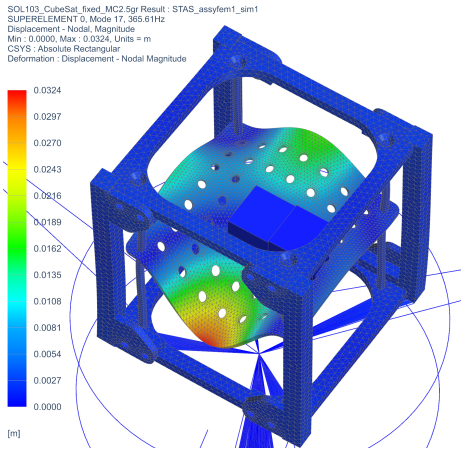


**Figure A.12:** $f_9$ of the CubeSat dummy model.

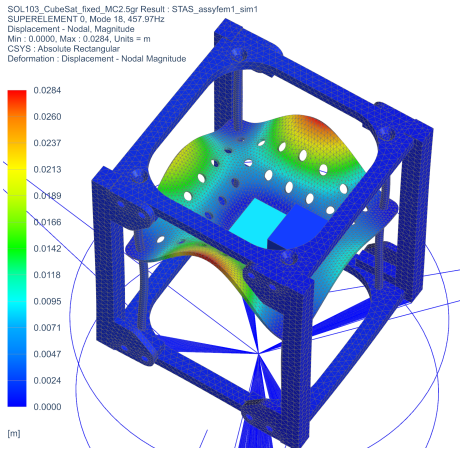


**Figure A.13:** $f_{10}$ of the CubeSat dummy model.

# Bibliography


[1] Singiresu S. Rao. *Mechanical Vibrations*. Reading, MA: Pearson, 2010 (cit. on pp. 1, 3, 5).

[2] Priscilla Long. *Tacoma Narrows Bridge collapses on November 7, 1940*. `https://www.historylink.org/File/5048`. HistoryLink.org, 2003, Essay 5048 (cit. on p. 3).

[3] Masterclass on enviromental Testing for Aerospace & Defence. "Vibration qualification testing of aerospace components and satellites". English. In: 2022 (cit. on pp. 6, 8).

[4] Umberto Musella, Davide Mastrodicasa, Stefania Grozavu, Mostapha Choukri, Simone Manzato, Marcos Chimeno, Ivan Ngan, Bart Peeters, and Alberto Garcia de Miguel. "Analysis of the vibro-acoustic interaction in direct field acoustic noise tests via optical measurement techniques". English. In: *Proceedings of ECSSMET 2024*. European Conference on Spacecrafts Structures Materials and Environmental Testing, ECSSMET 2024 ; Conference date: 23-09-2024 Through 27-09-2024. Proceedings of the European Conference on Spacecraft Structures, Materials and Environmental Testing, 2024. URL: `https://atpi.eventsair.com/ecssmet2024/proceedings-1` (cit. on pp. 6, 7, 11).

[5] Siemens Digital Industries Software. *What is vibration control testing?* `https://community.sw.siemens.com/s/article/what-is-vibration-control-testing`. 2020 (cit. on p. 7).

[6] Siemens Digital Industries Software Community. *Getting Started with Random Control*. `https://community.sw.siemens.com/s/article/Getting-Started-with-Random-Control`. 2023 (cit. on p. 9).

[7] Siemens Digital Industries Software. *Vibration Control: Understanding SelfCheck*. `https://community.sw.siemens.com/s/article/vibration-control-understanding-selfcheck`. 2019 (cit. on p. 9).

[8] Masterclass on enviromental Testing for Aerospace & Defence. "Dynamic Environmental testing of components". English. In: 2022 (cit. on p. 10).

[9] Masterclass on enviromental Testing for Aerospace & Defence. "More realistic, advanced and accelerated enviromental testing with MIMO technology". English. In: 2022 (cit. on p. 11).

[10] Massachusetts Institute of Technology (MIT). *The Virtual Motion Magnification (VMM) Project*. `https://people.csail.mit.edu/mrub/vidmag/` (cit. on p. 13).

[11] Tae-Hyun Oh, Ronnachai Jaroensri, Changil Kim, Mohamed Elgharib, Frédo Durand, William T Freeman, and Wojciech Matusik. "Learning-based Video Motion Magnification". In: *arXiv preprint arXiv:1804.02684* (2018) (cit. on p. 13).

[12] NASA/Tom Tschida. *AMF-EC02-0203-46*. Taken: August 22, 2002; Producer: AFRC; PIA Number: EC02-0203-46. URL: https://www.nasa.gov/image-detail/amf-ec02-0203-46/ (cit. on p. 14).

[13] Raphael Hallez. *Digital Image Correlation (DIC) for Aircraft GVT*. 2021. URL: https://blogs.sw.siemens.com/simcenter/digital-image-correlation-dic-for-aircraft-gvt (cit. on p. 14).

[14] Chittano Lorenzo. "From images to Modal Analisys via Phase-Based Motion Magnification and Estiamtion". MA thesis. Torino: Politecnico di Torino, 2024 (cit. on pp. 15–17).

[15] P. Burt and E. Adelson. "The Laplacian Pyramid as a Compact Image Code". In: *IEEE Transactions on Communications* 31.4 (1983), pp. 532–540. DOI: 10.1109/TCOM.1983.1095851 (cit. on p. 15).

[16] Neal Wadhwa, Michael Rubinstein, Fredo Durand, and William T. Freeman. "Riesz Pyramids for Fast Phase-Based Video Magnification". In: *2013 IEEE Conference on Computer Vision and Pattern Recognition (CVPR)*. Available at: https://people.csail.mit.edu/nwadhwa/phase-video-magnification/cvpr2013.pdf. Portland, OR, USA: IEEE, 2013, pp. 2291–2298. DOI: 10.1109/CVPR.2013.298 (cit. on pp. 18, 19).

[17] Justin G. Chen, Neal Wadhwa, Young-Jin Cha, Frédo Durand, William T. Freeman, and Oral Buyukozturk. "Structural Modal Identification Through High Speed Camera Video: Motion Magnification". In: *Proceedings of the Engineering Mechanics Institute International Conference (EMI International Conference)*. Available at: https://www.cs.cmu.edu/~wadhwa/Wadhwa_Chen_Cha_EMI_2014.pdf. McLean, VA, USA, 2014 (cit. on p. 18).

[18] Montesion Samuele. "Manufacturing and validation of 3D printed space structures via multi-axial testing". MA thesis. Torino: Politecnico di Torino, 2024 (cit. on p. 33).

[19] *User Manual Vega C*. AVIO S.p.A. 2025. URL: https://www.avio.com/sites/avio.com/files/downloads/UM%20Vega%20C%20-%20Iss1%20Rev0.pdf (cit. on pp. 36, 50).

[20] S. Corvaja and ESA. *Vega VV02 ready for liftoff*. https://www.esa.int/ESA_Multimedia/Images/2013/05/Vega_VV02_ready_for_liftoff. Image credit: ESA–S. Corvaja. 2013 (cit. on p. 36).

[21] Matthieu Vitse. *Blendic: Blender VTK Import Addon*. https://gitlab.com/sciviz/blendic. Version: 1.2.0, Last updated: 2020-10-10 (cit. on pp. 39, 42).

*To my family*,
especially to my parents, who have allowed me to cultivate my passion for science and technology without hesitation, never sparing any effort or expense, and never putting pressure on me. This thesis may serve as a token of my gratitude for all the support and trust you have given me.

*To my sister*,
who has paved the way ahead of me and taught me that success is important, but also that it requires time and sacrifice. She has shown me the value of taking the time to choose one's path thoughtfully, of being a good listener, and of offering advice at the right moment. Even though I have never told her directly, she has always been my role model.

*To my girlfriend*,
who has endured both highs and lows with me over the past two years, yet has always known how to lift me up during difficult moments and helped me discover sides of life I would have never encountered without her.

For the sake of brevity, I will not go into detail — but if you wish to know what I am grateful for, please feel free to ask me in person.

*To all the people who are here today, and to those who could not be*,
with whom I have shared moments, experiences, and growth in many different forms. To those I have met through friendship, and to those who, even if no longer part of my everyday life, have left a lasting mark. To those who have stayed, and with whom those friendships have only grown stronger.

I thank you all sincerely for being part of my journey.